Key Points:
- CPO evolution of olivine polycrystals is modeled using D-Rex and VPSC.
- Deformation history significantly influences texture evolution in olivine polycrystals.
- Long-lived transient CPOs provide new ways to interpret seismic anisotropy in terms of mantle flow

Correspondence to:
Y. Boneh,
boneh@levee.wustl.edu

Modeling olivine CPO evolution with complex deformation histories: Implications for the interpretation of seismic anisotropy in the mantle

Yuval Boneh[1], Luiz F. G. Morales[2], Edouard Kaminski[3], and Philip Skemer[1]

[1]Department of Earth and Planetary Sciences, Washington University in St. Louis, Saint Louis, Missouri, USA, [2]GFZ German Research Centre for Geosciences, Potsdam, Germany, [3]Institut de Physique du Globe de Paris, Sorbonne Paris Cité, Université Paris Diderot, CNRS, Paris, France

Abstract Relating seismic anisotropy to mantle flow requires detailed understanding of the development and evolution of olivine crystallographic preferred orientation (CPO). Recent experimental and field studies have shown that olivine CPO evolution depends strongly on the integrated deformation history, which may lead to differences in how the corresponding seismic anisotropy should be interpreted. In this study, two widely used numerical models for CPO evolution—D-Rex and VPSC—are evaluated to further examine the effect of deformation history on olivine texture and seismic anisotropy. Building on previous experimental work, models are initiated with several different CPOs to simulate unique deformation histories. Significantly, models initiated with a preexisting CPO evolve differently than the CPOs generated without preexisting texture. Moreover, the CPO in each model evolves differently as a function of strain. Numerical simulations are compared to laboratory experiments by Boneh and Skemer (2014). In general, the D-Rex and VPSC models are able to reproduce the experimentally observed CPOs, although the models significantly over-estimate the strength of the CPO and in some instances produce different CPO from what is observed experimentally. Based on comparison with experiments, recommended parameters for D-Rex are: $M^* = 10$, $\lambda^* = 5$, and $\chi = 0.3$, and for VPSC: $\alpha = 10$–100. Numerical modeling confirms that CPO evolution in olivine is highly sensitive to the details of the initial CPO, even at strains greater than 2. These observations imply that there is a long transient interval of CPO realignment which must be considered carefully in the modeling or interpretation of seismic anisotropy in complex tectonic settings.

1. Introduction

Patterns of flow in Earth's interior provide insight into the convective forces that drive plate motions. However, flow patterns are difficult to determine uniquely as Earth's interior is largely invisible to direct observation. Geophysical data, such as the velocity and anisotropy of seismic waves, represent our primary window into the internal structure of the planet. In the upper mantle, anisotropy of seismic wave velocities is caused mainly by the preferential alignment of seismically anisotropic grains in polycrystalline rock—often called crystallographic preferred orientation (CPO). CPO develops through the activity of specific deformation mechanisms, which cause individual crystal lattices to rotate into favored orientations with respect to the kinematics of flow [*Ave Lallemant*, 1975; *Nicolas and Christensen*, 1987].

Models of CPO evolution provide tools to both predict and interpret seismic anisotropy. This can be implemented in a forward manner by coupling geodynamic flow simulations or physical models to a numerical or conceptual model for CPO evolution, leading to predictions for seismic anisotropy in a given setting [*Blackman et al.*, 1996; *Chastel et al.*, 1993; *Conrad et al.*, 2007; *Druken et al.*, 2011, 2013; *Faccenda and Capitanio*, 2012, 2013; *Paczkowski et al.*, 2014; *Tommasi*, 1998]. CPO modeling can also be applied in an inverse way to relate seismological observations to the kinematics of mantle flow [*Alpert et al.*, 2013; *Becker et al.*, 2006b].

To interpret seismic anisotropy in terms of mantle flow it is typically assumed that CPO is near steady state, which means that the current CPO reflects the macroscopic deformation kinematics of the region sampled by the seismic waves. This assumption implies that the rate of CPO evolution along a particular flowline is significantly smaller than the rate of deformation evolution, as quantified by the Grain-Orientation-Lag

(GOL) parameter introduced by *Kaminski and Ribe* [2002]. *Boneh and Skemer* [2014] proposed an additional set of empirical criteria for determining whether steady state CPO has been achieved. Texture can be considered in steady state if the strength, symmetry, and orientation of the crystallographic orientation patterns do not change with progressive strain. Using similar criteria, recent experiments on polycrystalline olivine show that very large strains are necessary (up to a shear strain of 10) in order to achieve textural steady state [*Hansen et al.*, 2014]. Experiments and field observations have also demonstrated that preexisting textures introduced by complex deformation histories significantly modify the rate and patterns of subsequent CPO evolution [*Boneh and Skemer*, 2014; *Skemer et al.*, 2010, 2011; *Warren et al.*, 2008; *Webber et al.*, 2010]. These studies demonstrate that there is considerable variability in the rate of texture development, especially in comparison to experiments that do not take into account preexisting texture [*Skemer et al.*, 2012]. Furthermore, experiments by *Hansen et al.* [2012] have demonstrated that the shear strength of polycrystalline olivine is a function of texture strength, confirming that microstructure and rheology are coupled up to very large strains [*Knoll et al.*, 2009]. Collectively, these data corroborate inferences from natural shear zones, which are thought to experience long transient evolution of both microstructure and rheology.

The protracted evolution of olivine CPO suggests that deformation history should have a significant impact on the interpretation of seismic anisotropy [*Kaminski and Ribe*, 2002; *Skemer et al.*, 2012]. The viability of the forward modeling approach is contingent on the capability of numerical models to simulate CPO evolution with complex deformation history. A wide range of theoretical models using different physical backgrounds and hypotheses have been proposed to simulate texture evolution, including the viscoplastic self-consistent approach [*Lebensohn and Tomé*, 1993; *Tommasi et al.*, 2000; *Wenk et al.*, 1991], second order viscoplastic self-consistent approach [*Castañeda*, 2002; *Raterron et al.*, 2014], the kinematic model D-Rex [*Kaminski and Ribe*, 2001; *Kaminski et al.*, 2004], and equilibrium-based models [*Chastel et al.*, 1993]. In many cases, these models have been parameterized through comparison with laboratory experiments, such as the results of *Nicolas et al.* [1973] and *Zhang and Karato* [1995], which describe the formation and evolution of olivine deformed in uniaxial compression and simple shear, respectively. However, a limitation of these comparisons is that the starting materials of most of laboratory experiments and corresponding simulations have a "random" texture, in which there is no significant quantifiable alignment of grains. Indeed, it is challenging to model CPO evolution with complex deformation histories and kinematics [*Blackman and Kendall*, 2002; *Castelnau et al.*, 2009], which contributes to the difficulty of interpreting seismic anisotropy near plate boundaries [e.g., *Becker et al.*, 2014; *Blackman*, 2007; *Castelnau et al.*, 2009].

In this study we compare numerical models of CPO evolution with recent experimental results that demonstrate the effect of deformation history on CPO [*Boneh and Skemer*, 2014]. We employ two widely used methods for texture development modeling: the viscoplastic self-consistent (VPSC) approach as described in *Tommasi et al.* [2000], which is based on the reorientation of crystals through intracrystalline slip and grain interactions, and the D-Rex approach [*Kaminski and Ribe*, 2001], which considers intracrystalline slip and dynamic recrystallization but does not model mechanical interactions between grains. The VPSC approach has been used to simulate olivine texture in mantle flow, shear zones and lithospheric plate interactions [*Bonnin et al.*, 2012; *Di Leo et al.*, 2014; *Li et al.*, 2014; *Tommasi et al.*, 1999, 2009]. D-Rex is often used to simulate larger strains, when dynamic recrystallization must be taken into account. D-Rex is also preferred in larger-scale geodynamic models, due to its relative ease of computation [*Becker et al.*, 2006a; *Conder and Wiens*, 2007; *Faccenda and Capitanio*, 2012; *Hedjazian and Kaminski*, 2014; *Kaminski and Ribe*, 2002]. In contrast to the standard approach of comparing CPO evolution in experiments and models with a random set of initial grain orientations, we have initiated our models using the same natural CPO and the same deformation configurations previously explored experimentally by *Boneh and Skemer* [2014]. This approach allows for the direct comparison between experiments and numerical modeling and provides new insights about the effect of preexisting crystallographic orientation on the texture development.

2. Methods

Both VPSC and D-Rex models are described extensively elsewhere [*Kaminski and Ribe*, 2001; *Kaminski et al.*, 2004; *Lebensohn and Tomé*, 1993; *Tommasi et al.*, 2000]. Here we will highlight only the main features and differences between these models. For both models, the rotation of grains is implemented through the

glide of dislocations along specific crystal slip systems. The models consider the experimentally determined olivine slip systems and their critical resolved shear stress (CRSS); deformation follows the viscoplastic law:

$$\dot{\gamma}_s = \dot{\gamma}_0 \left(\tau_r^s / \tau_0^s \right)^n \tag{1}$$

$\dot{\gamma}_s$ is the slip system strain-rate, $\dot{\gamma}_0$ is the reference strain-rate, τ_r^s is the resolved shear stress (a function of the Schmidt factor—the orientation of the slip system with respect to the imposed stress), τ_0^s is the critical resolved stress, and n is the stress exponent.

2.1. D-Rex Model

Modeling texture through the kinematic approach of D-Rex assumes crystal reorientation through the local velocity gradient:

$$d_{ij} = G_{ij}v - \varepsilon_{ijk}w_k \tag{2}$$

where Gij is the Schmidt factor, which relates the crystal and imposed stress orientations, v is the slip rate on the softest slip system for a given grain, ε_{ijk} is the macroscopic (aggregate) strain rate, and ω is the rotation rate. In order to satisfy the strain compatibility a minimization technique is used to minimize the difference between the single crystal and aggregate strain [*Ribe and Yu*, 1991]. The residual strain, ∼10% [*Kaminski and Ribe*, 2001], is assumed to be accounted for by processes that do not impose crystal rotation, such as diffusive mass transfer and/or grain boundary migration [*Ribe and Yu*, 1991].

D-Rex simulates dynamic recrystallization through two dimensionless parameters that account for grain boundary migration and grain nucleation (*M** and *λ** respectively). D-Rex also simulates the effects of "grain boundary sliding" through the dimensionless parameter χ [*Kaminski et al.*, 2004]. Grain growth is incorporated using a parameter for grain-boundary migration:

$$M^* = \frac{A\mu b M}{\upsilon} \tag{3}$$

where A is dimensionless constant, μ is the shear modulus, b is Burger vector, M is a dimensionless grain-boundary mobility, and υ is the dislocation velocity.

Grain size reduction through dynamic recrystallization is incorporated into D-Rex using a parameter for the nucleation of strain-free grains

$$\lambda^* = \ln(\alpha_V) \left(\frac{\rho_0}{\rho} \right) \tag{4}$$

where λ^* is dimensionless nucleation parameter, α_V is the nonrecrystallized volume fraction of the crystal, and ρ_0 and ρ are a reference dislocation density and the crystal's dislocation density, respectively, the ratio of which acts as the driving force for nucleation. The two parameters, *M** and *λ**, account for competing processes. *M** is responsible for the migration of grain boundaries, which cause highly strained crystals ("soft" grains) to be invaded by weakly strained crystals ("hard" grains) increasing the number of grains in hard orientations. *λ** accounts for the nucleation of new grains, which cause the highly strained soft grains to nucleate new grains with zero strain in the same orientation. Due to their low stain energy, these grains then grow by grain boundary migration, increasing the volume fraction of grains in soft orientations. One effect of grain size reduction by nucleation of new small grains is that these grains may accommodate strain by mechanisms that do not invoke crystallographic rotation (diffusion creep and/or grain boundary sliding). This effect is represented by parameter χ, which disables the rotation of grains below a specific grain volume fraction threshold [*Kaminski et al.*, 2004].

2.2. VPSC Model

In the VPSC approach, each grain's strain and stress is considered in terms of the bulk aggregate strain and stress by using the "one site" grain interaction simplification which simulates interaction of each grain with a surrounding homogeneous equivalent medium (HEM) [*Eshelby*, 1957]:

$$\dot{\epsilon}_{ij} - \dot{E}_{ij} = -\alpha M_{ijkl}(s_{kl} - \Sigma_{kl}) \tag{5}$$

Where $\dot{\epsilon}_{ij}$ is the grain strain-rate, $\dot{E}_{ij}$ is the average strain-rate of the aggregate, α is parameter that describes grain interaction with its surroundings, M_{ijkl} is the interaction tensor that includes grain rheology and shape, s_{kl} is the grain deviatoric stress, and Σ_{kl} is the average stress of the aggregate. Through this approach, microscopic stress and strain rates may vary significantly with respect to the averaged (macroscopic) values. The grain interaction parameter, α, represents the grain response and ranges between the upper bound, in which α is equal to zero and homogeneous strain is assumed [*Taylor*, 1938], and the lower bound, in which α approaches infinity, and homogeneous stress is assumed [*Sachs*, 1928]. Limitations of the VPSC compared to full-field models (models that include aggregate microstructure) have been shown, in particular, the effect of secondary slip systems [*Castelnau et al.*, 2008; *Castelnau et al.*, 2010; *Detrez et al.*, 2015] and the overestimation of texture strength [*Castelnau et al.*, 2006].

2.3. Differences Between VPSC and D-Rex

The fundamental difference between VPSC and D-Rex is that the former is physics-based (mean-field) model while the latter is an ad hoc (far-field) model. In VPSC interaction between grains are considered via the HEM assumption while stress compatibility is maintained, which allows a meaningful representation of the relative activity of different slip system [*Tommasi et al.*, 2000]. The formulation of the VPSC approach in the present study does not include processes like dynamic recrystallization or relaxation processes like dislocation climb and grain boundary sliding, although this has been implemented recently by *Signorelli and Tommasi* [2015]. In contrast, D-Rex includes ad hoc parameters that are intended to simulate microphysical processes in addition to deformation: dynamic recrystallization and grain boundary sliding. In addition, the calculation of intracrystalline deformation in D-Rex is analytical. Hence the code requires fewer computations, which allows it to be easily coupled to larger geodynamic models.

2.4. Model Starting Conditions

Both VPSC and D-Rex models are initiated using input textures composed of 1000 grain orientations. In some tests, simulations are initiated using random crystal orientations. In most of the present study however, we use the CPO of a natural dunite from Åheim, Norway as the starting texture. This is the CPO of the same rock specimen that we used as the starting material for the experiments of *Boneh and Skemer* [2014] and has been widely used in other rock mechanics studies [*Chopra and Paterson*, 1981, 1984; *Jackson et al.*, 1992; *Keefner et al.*, 2011; *Van der Wal et al.*, 1993; *Wendt et al.*, 1998]. The texture of the Åheim dunite was measured by Electron Backscatter Diffraction (EBSD), (for details of microstructural characterization, see *Boneh and Skemer* [2014]). The Åheim dunite is foliated and exhibits a strong axial girdle (AG) texture, characterized by the alignment of [010] axes normal to the foliation of this rock, while [100] and [001] are distributed along single continuous girdles parallel to the foliation (Figure 1a). Such a pattern reflects a history of nearly uniaxial deformation [*Mainprice*, 2015; *Nicolas et al.*, 1973; *Wenk et al.*, 1991]. In both the *Boneh and Skemer* [2014] experiments and in the models described in this study, the Åheim dunite texture (Figure 1a) was deformed in three different configurations in which the sample and/or CPO is rotated to angles of 0, 45, and 90 degrees with respect to the shortening axis (Figure 1b).

The stress exponent used in the models (n = 3.5, Table 1) has been well established by rock deformation experiments for olivine single crystals in various orientations [*Bai et al.*, 1991; *Durham and Goetze*, 1977], as well as for polycrystals [*Karato et al.*, 1986]. To maintain consistency and to facilitate comparison with previous studies, the relative strength of olivine's primary slip-systems for VPSC and D-Rex (Table 1) are taken from *Tommasi et al.* [2000] and *Kaminski and Ribe* [2001], respectively. These critical resolved shear stresses are chosen to represent the most ubiquitous olivine texture (A-type, of *Jung and Karato* [2001]), which is dominated by slip on the [100](010) slip system [*Ben Ismaïl and Mainprice*, 1998]. The [100](010) slip system is also inferred to be the dominant slip system in the *Boneh and Skemer* [2014] experiments. The deformation geometry is uniaxial compression with the corresponding strain tensor with $\varepsilon_{11} = \varepsilon_{33} = 0.5$, $\varepsilon_{22} = -1$ and $\varepsilon_{i \neq j} = 0$. The parameters used are $\alpha = 100$ for VPSC, and $M^* = 10$, $\lambda^* = 5$, $\chi = 0.3$, for D-Rex. Rationale for this choice of parameters is discussed in section 4.2.

2.5. Quantifying Texture and Anisotropy

Texture is characterized by its strength, its symmetry, and its orientation with respect to the reference frame of deformation. Texture symmetry and orientation control the orientation of anisotropy detected seismologically. Texture strength influences mainly the magnitude of the anisotropy up to a limit, after which the magnitude reaches saturation [*Hedjazian and Kaminski*, 2014].
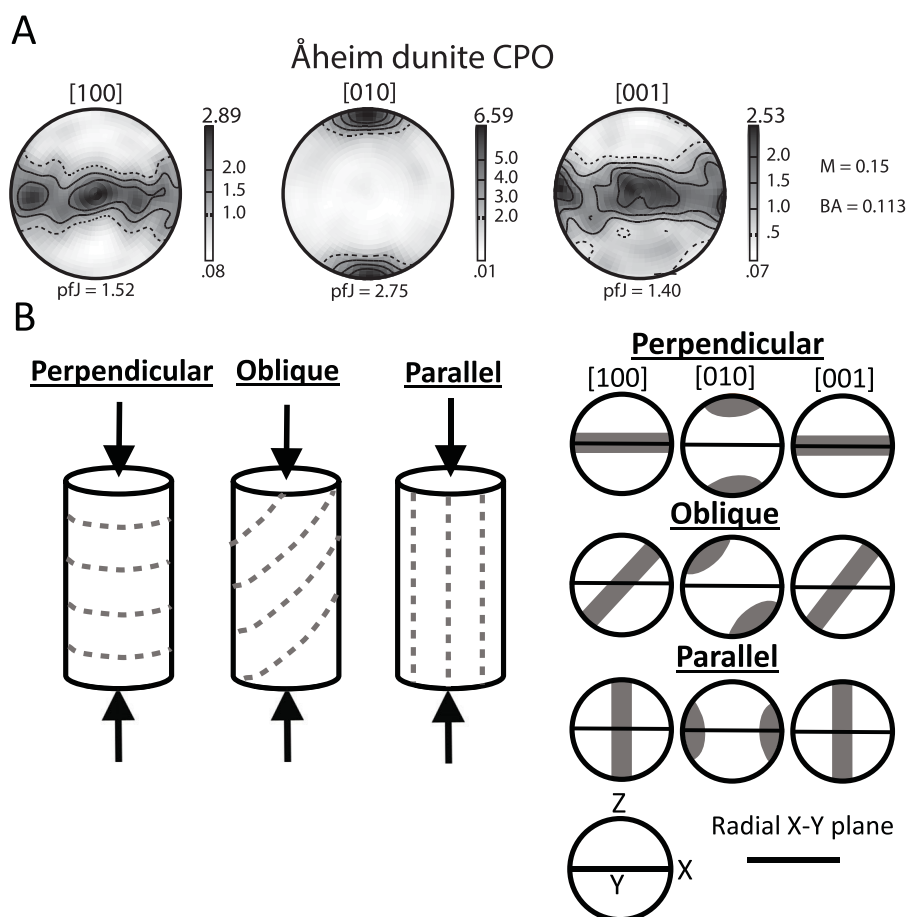
Figure 1. (a) Pole figures showing the olivine crystallographic preferred orientation (CPO) of Åheim dunite. The Åheim dunite exhibits a girdle of orientations in [100] and [001] parallel to the foliation plane. The foliation is also marked as dotted lines in Figure 1b. Contour intervals are linear and scaled to multiples of uniform distribution, m.u.d. (scale bars on left side of each pole figure). Texture strength (M-index) and texture symmetry (BA-index) are listed to the right of the pole figures. (b) Three configurations of the Åheim dunite samples in which the axis of shortening is perpendicular, oblique, or parallel to the dunite initial foliation. On the right are schematic illustrations of the initial texture for each of the three configurations. Pole figures are in a X-Y-Z reference frame in which the shortening axis is parallel to the Z direction and the X-Y plane is in the radial plane, perpendicular to the shortening axis.

In order to evaluate texture evolution with increasing strain we use several quantitative parameters. Texture strength is quantified using the M-index method, ranging from M = 0, for a perfect random texture, to M = 1, for perfect crystallographic alignment (e.g., a single grain) [*Skemer et al.*, 2005], and the pole figure strength (pfJ) parameter [e.g., *Mainprice et al.*, 2014] for individual pole figures, which ranges from 1 for a perfect random texture to infinity for perfect alignment. As [100], [010] and [001] are all two-fold rotation axes, the results from pfJ can be directly compared.

Table 1. Models Input Parameters

Slip System	VPSC CRSS[a]	D-Rex CRSS[a]
(010)[100]	1	1
(001)[100]	1	2
(010)[001]	2	3
(100)[001]	3	6
(021)[100]	6	
(110)[001]	6	
n (stress exponent)[b]	3.5	3.5
N (number of grains)	1000	1000

[a]CRSS––Relative Resolved Shear Stress. The CRSS is relative to the weakest slip system ((010)[100]).
[b]the same stress exponent was used for all slip systems.

Texture symmetry is quantified using the parameters Point (P), Girdle (G), and Random (R), which describe whether the CPO is best represented by a point maximum (Point), an equal distribution of points along a plane (Girdle), or a uniformly distributed texture with no preferred orientation (Random) [*Vollmer*, 1990]. These three symmetry parameters, calculated from eigenvalues of the orientation tensor [*Mainprice et al.*, 2014], always sum to 1, and therefore can be plotted in a ternary diagram [e.g., *Falus et al.*, 2011; *Higgie and Tommasi*, 2012; *Morales and Tommasi*, 2011;
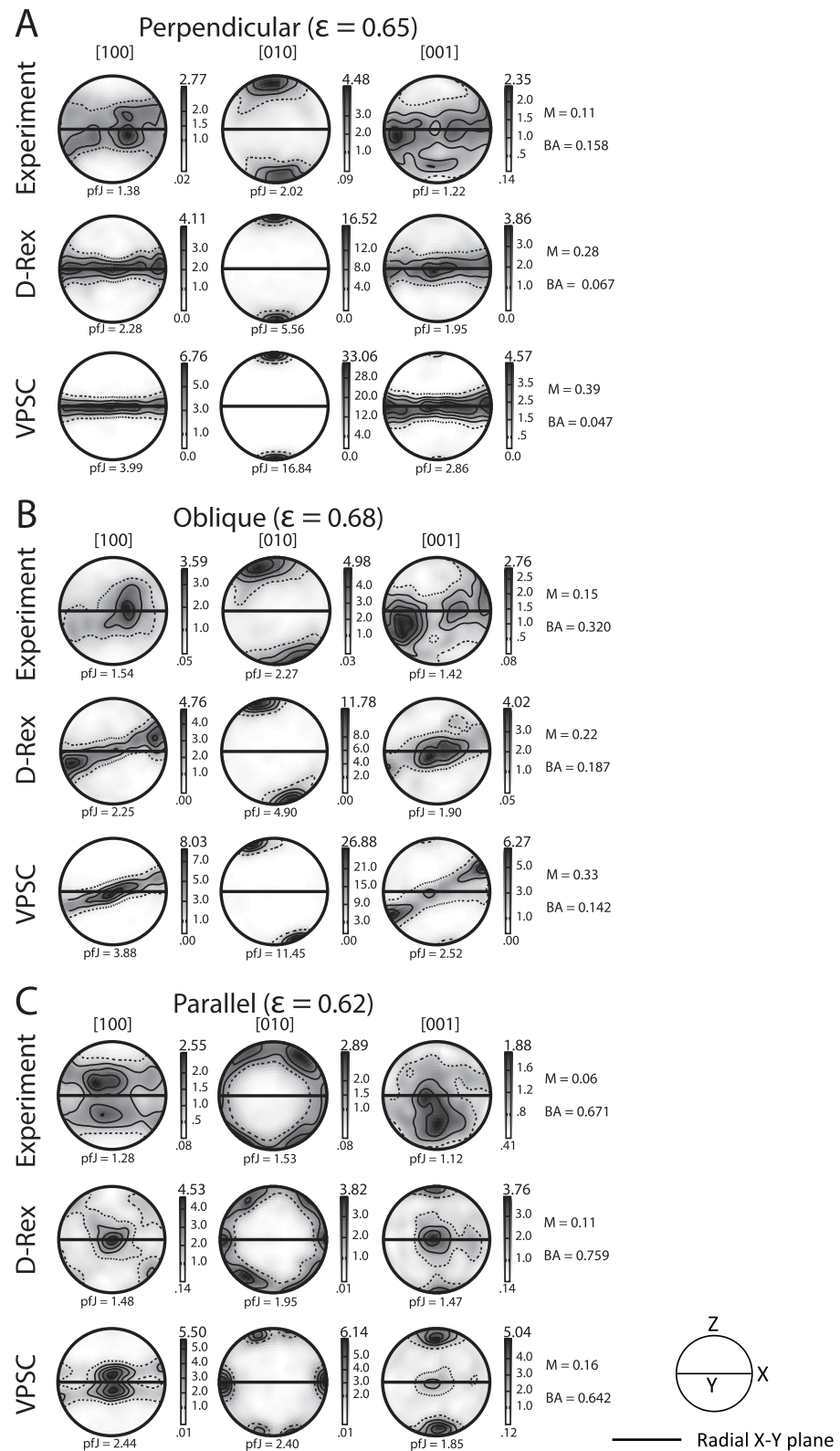
Figure 2. Pole figures showing texture from experiments, VPSC, and D-Rex models for the three starting configurations: (a) perpendicular, (b) oblique, and (c) parallel. Experimental data are taken from high strain experiments of *Boneh and Skemer* [2014]. Parameters used in models: for D-Rex: M* = 10, λ* = 5, χ = 0.3, and for VPSC: α = 100 (other parameters are shown in Table 1). Scale bar to the right of each pole figure show the multiples of uniform distribution (m.u.d.). Pole figures projected in equal area and lower hemisphere. Texture strength of each pole figure (pfJ), the total texture strength (M-index), and the texture symmetry (BA-index) are given.

Tommasi et al., 2008; *Vauchez et al.*, 2005]. P, G, and R components for specific pole figures are denoted using subscript notation: (e.g., the girdle component of the [100] pole figure is denoted $G_{[100]}$). Another way to quantify a specific coaxial texture is the BA-index, in which a specific point and girdle components are compared to the point and girdle sum so that the dependence of the texture symmetry on the random component is minimized:

$$BA = 0.5 \left[2 - \left(\frac{P_{010}}{G_{010} + P_{010}} \right) - \left(\frac{G_{100}}{G_{100} + P_{100}} \right) \right] \tag{6}$$

The BA-index represents symmetry that includes point maxima in the [010] and girdle in the [100] and is scaled to range from BA = 0 to BA = 1 [*Mainprice et al.*, 2014]. BA = 0 corresponds to a "perfect" axial girdle (AG) texture while BA = 1 would represent the absence of an AG texture.

Pole figures of CPO and seismic velocities were calculated and plotted using D. Mainprice software (Petrophysical software, Unicef Careware, http://www.gm.univ-montp2.fr/PERSO/mainprice/) [*Mainprice*, 1990], which assumes Voigt-Reuss-Hill average and elastic constants for olivine from *Abramson et al.* [1997] in calculating the seismic velocities. We also apply a code by *Savransky and Kasdin* [2012] to convert grains orientations output from directional cosines [*Kaminski and Ribe*, 2001, equation (1)] to Euler angles. Pole figures of CPO used for Movie S1 (supporting information) were generated using MTEX [*Bachmann et al.*, 2010; *Mainprice et al.*, 2011].

3. Results

3.1. CPO Development With Different Starting Textures

In Figure 2, CPOs generated by D-Rex and VPSC models are compared with the experiments of *Boneh and Skemer* [2014]. Results are shown for the three initial configuration: perpendicular (Figure 2a), oblique (Figure 2b), and parallel (Figure 2c). Models are run to the same finite strains achieved experimentally (0.65, 0.68, and 0.62, for the three configurations, respectively).

In the perpendicular configuration (Figure 2a), the experimental texture exhibits a fiber texture (i.e., the coaxial AG-fabric) with girdles in [100] and [001] and a strong point maxima of [010], which is similar to the initial texture symmetry (Figure 1a). Both models show significantly stronger texture than the experiments. For example, the [010] axes in the experimental CPO have a pole figure J-index strength (pfJ) of ~2 compared to 5.5 in D-Rex and almost 17 in VPSC.

In the oblique configuration (Figure 2b), the experimental texture shows the [010] point maximum rotated from its original position toward the shortening direction, and weak [100] and [001] point maxima. Both models predict a [010] point maximum rotation similar to the experiment, however, there is difference in the strength of this point maximum ([010] pfJ of 2.27, 4.9 and 11.45 for the experiments, D-Rex, and VPSC, respectively). In the experiments, D-Rex, and VPSC models, there is a pronounced [100] point maximum superimposed on a girdle in the axial plane, giving the texture a pseudo-orthorhombic symmetry.

In the parallel configuration, the experimental texture shows a weak [100] girdle along the radial (X-Y) plane, a [010] girdle along the X-Z plane, and a very weak CPO, i.e., mostly random texture, in the [001] axis (pfJ of 1.12). Both models predict that the [010] axes are distributed along the X-Z plane with three distinct point maxima (one in the X direction and two at a symmetric and oblique angle away from the shortening axis). These three point maxima are more diffuse in D-Rex than in VPSC. For the [100] axis, D-Rex shows a point maximum parallel to Y with two weaker bands of data oriented in an "x" shape at a high angle to the radial plane. VPSC shows a stronger point maximum toward Y with "x" shaped bands forming a girdle subparallel to the radial plane. The "x" shaped features in the model's CPO agree well with the experimental observations, although there is a difference in the strength and orientation of the bands. For the [001] axis, both VPSC and D-Rex have similar textures with two point maxima at the Y and Z directions. The models predict two point maxima in the [001] axis, parallel to the X and Y axis, but the experiments show a disperse crystals oriented only toward Y axis (also among other strains in the parallel configurations, see *Boneh and Skemer* [2014, Figure 3c]).

3.2. Evolution of Texture Symmetry

D-Rex and VPSC models were run over a range of strains to assess how CPO evolves as a function of strain. Texture evolution for D-Rex (square symbols) and VPSC (circle symbols) models are shown in Figure 3 using
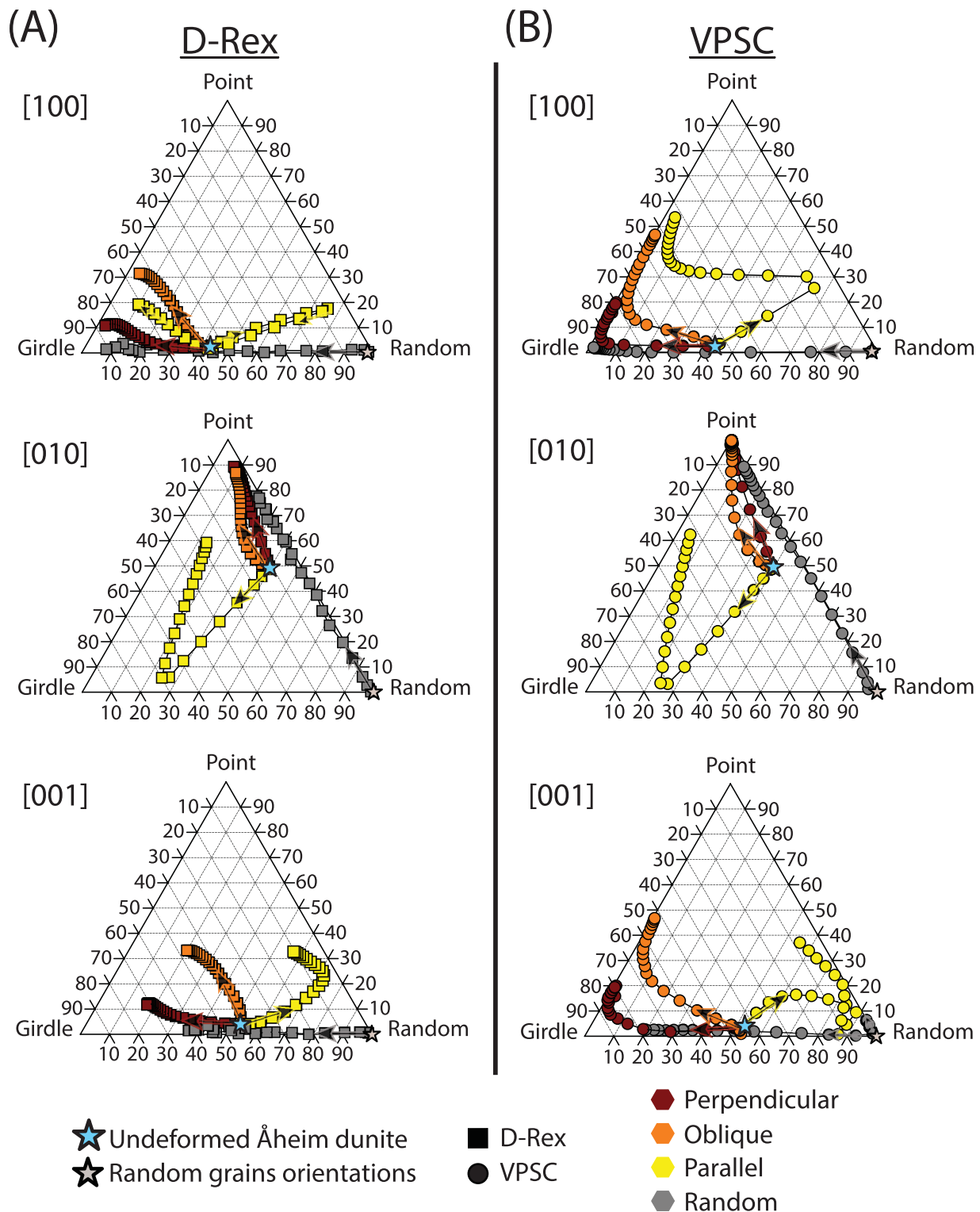
Figure 3. Ternary diagram of texture symmetry parameters Point, Girdle and Random, calculated using eigenvalues of the orientation tensor [*Vollmer*, 1990], for: (a) D-Rex (square symbols), and (b) VPSC (circles symbols). There are total of 22 strain steps: $\varepsilon = 0.01$ and 0.05, and 20 steps in increments of 0.1 (from $\varepsilon = 0.1$ to 2). Three models with preexisting configurations are shown: perpendicular (dark red), oblique (orange), and parallel (yellow), and an initially un-textured case is shown for reference (gray). The stars denote the two starting conditions: the undeformed Aheim dunite in blue and the untextured scenario in gray. Arrows show the initial trend of symmetry development from the initial texture. The symmetry of each configuration is shown to evolve differently as a function of strain.

a ternary diagram with Point, Girdle and Random texture components as end members. For each of olivine's three crystallographic axes the symmetry trajectory is shown for the three configurations with preexisting texture: perpendicular (dark red symbols), oblique (orange symbols), and parallel (yellow symbols), and for an initially random texture (gray symbols). Each point represents a strain-increment between the initial textures, with strain of zero, to strain of 2. The first two points represent texture for small finite strains of 0.01 and 0.05, while the next 20 points are equally spaced with strain intervals of 0.1 (between strain of 0.1–2). The starting point (i.e., strain = 0) from which texture evolves for the three configurations with preexisting texture is shown as a blue star. The starting point for the random case, shown as gray star, is defined as having symmetry of R = 1, and P = G = 0.

For models initiated with random texture D-Rex and VPSC produce similar results, which are essentially identical to the results of *Kaminski and Ribe* [2001] and *Tommasi et al.* [2000]. Texture evolves from random to girdle in [100] and [001], and from random to point in [010], as expected from the experimental results of *Nicolas et al.* [1973]. In the D-Rex model, $G_{[100]}$ increases from 0 to 0.91, $P_{[010]}$ increases from 0 to 0.78, while $G_{[001]}$ increases from 0 to 0.60. In the VPSC model, $G_{[100]}$ increases from 0 to 0.96, $P_{[010]}$ increases from 0 to 0.89, while $G_{[001]}$ increases from 0 to 0.78.

For models initiated with preexisting texture, each of the three pretextured configurations shows different symmetry evolution and they also evolve differently with respect to the initially un-textured scenario. For the D-Rex models, $G_{[100]}$ increases from 0.54 to 0.87, 0.64, and 0.71 for perpendicular, oblique and parallel configuration, respectively, $P_{[010]}$ increases from 0.49 to 0.89, 0.87, and 0.59 for perpendicular, oblique and parallel configuration, respectively. For the VPSC models $G_{[100]}$ evolves from 0.54 to 0.80, 0.53, and 0.43 for perpendicular, oblique and parallel configuration, respectively. $P_{[010]}$ increases from 0.49 to 0.99, 0.99, and 0.62 for perpendicular, oblique and parallel configuration, respectively.

D-Rex and VPSC show some notable differences in terms of their prediction of texture evolution. CPOs generated by the VPSC approach tend to evolve more quickly than CPOs generated by D-Rex. For example, in D-Rex the [100] axes in perpendicular and oblique configurations reach texture with Random parameter of $R_{[100]} < 0.05$ at 1.7 and 1.9 strain, respectively, while in VPSC $R_{[100]}$ requires strains of only 0.4 and 0.7, respectively. This effect is seen for the perpendicular and oblique configurations in the [001] axis as well. However, for the [010] axes the two models predict similar texture trajectories. The full set of texture data used in these calculations can be found in supporting information Tables S1 and S2. In addition, direct qualitative comparisons of CPO evolution between the two models can be made using the animation provided (supporting information Movie S1).

3.3. Texture Strength and Anisotropy

In order to further quantify the evolution of texture we calculate the total texture strength, using the M-index parameter [*Skemer et al.*, 2005], and the maximum P-wave seismic anisotropy. The calculated texture strength and the associated seismic anisotropy are plotted as a function of strain (Figure 4). Experimental data from *Boneh and Skemer* [2014] are shown as open symbols for comparison. Texture strength in D-Rex (Figure 4a) for the perpendicular and oblique configurations show a small gradual increase of texture strength to values of M = 0.36 and M = 0.31, respectively (Figure 4a), while the parallel configuration decreases slightly to a low and relatively constant value of M = 0.13. Texture strength in VPSC (Figure 4b) for the perpendicular configuration shows an initial increase of strength up to strain of about 0.75 then a steady strength value until strain of 2 (M = 0.45 at $\varepsilon = 2$). For the oblique configuration the strength increases throughout the strain range (M = 0.55 at $\varepsilon = 2$). For the parallel configuration strength decreases initially and starts to increase again when the strain is about 1 (M = 0.37 at $\varepsilon = 2$). Texture strength of the initially random case after strain of 2 is slightly higher (D-Rex) or similar (VPSC) to the parallel configuration strength at the same strain (which is significantly lower than the perpendicular and oblique configurations). The texture strength in both models is stronger in the perpendicular and oblique configurations than in the parallel configuration.

In Figures 4c and 4d, the P-wave seismic anisotropy in percentage (AVp = 200 $(Vp_{max} - Vp_{min})/(Vp_{max} + Vp_{min})$) is shown with respect to strain for D-Rex and VPSC, respectively. In both models the trend of increasing seismic anisotropy with strain is similar although the models differ in terms of the magnitude of the anisotropy. Seismic anisotropy in D-Rex for the perpendicular and oblique configurations show a small gradual increase of texture strength to almost similar values of AVp = 14.8% and AVp = 15.5%,

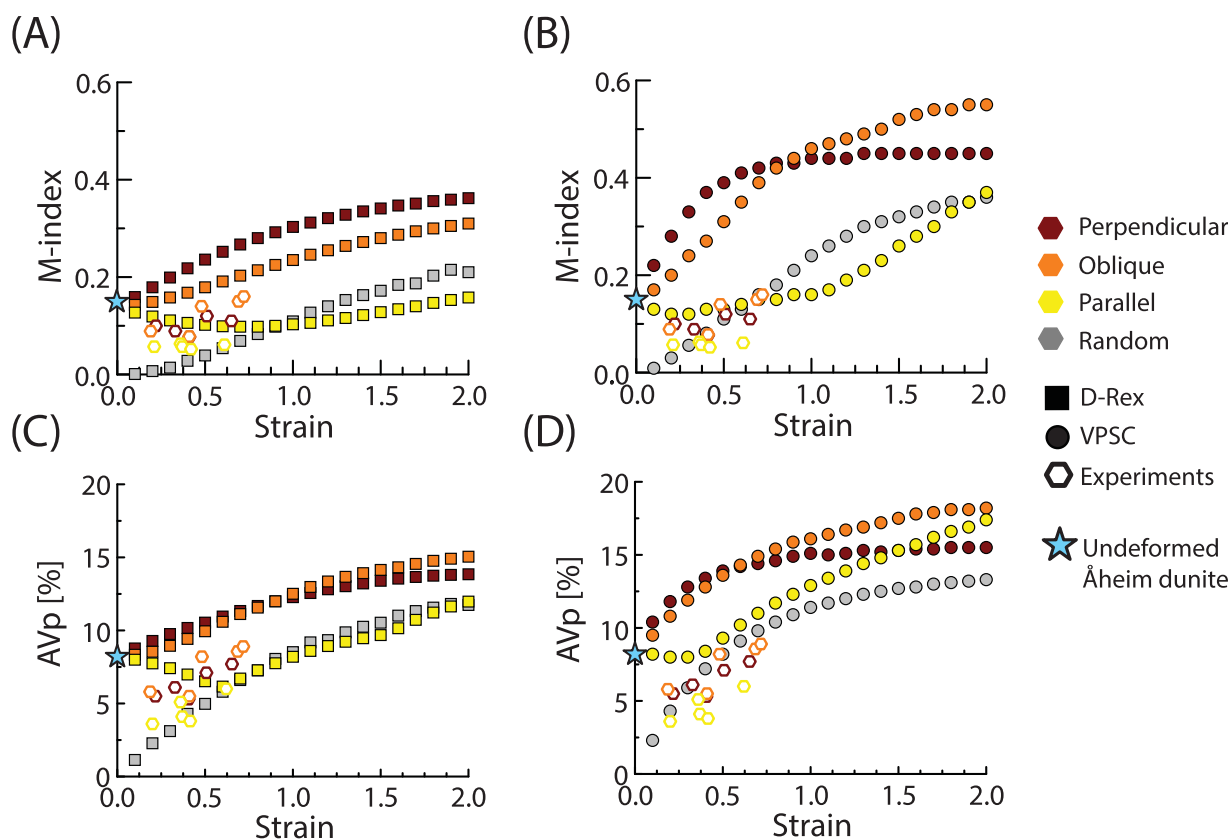**Figure 4.** (a and b) Texture strength and (c and d) P-wave seismic anisotropy (AVp = 200 (Vp$_{max}$−Vp$_{min}$)/(Vp$_{max}$ + Vp$_{min}$)) plotted as a function of strain. Numerical models are shown using solid symbols. Experimental data from *Boneh and Skemer* [2014] are shown as open symbols. Color denotes the configuration of the experiment or model: gray for initial random texture, dark red, orange, and yellow for perpendicular, oblique and parallel configuration, respectively. Blue star denotes the undeformed Åheim dunite. Texture strength is quantified using M-index [*Skemer et al.*, 2005]. Seismic anisotropy quantified using the maximum anisotropy of the P-wave velocity, in percent.

respectively (Figure 4d), while the parallel configuration initially decreases to AVp = 4.6% at strain of 0.5 then increases up to AVp = 13.3% at strain of 2. Seismic anisotropy in VPSC for the perpendicular and oblique configurations shows a small gradual increase of texture strength to values of AVp = 15.5% and AVp = 18.2%, respectively (Figure 4c), while the parallel configuration the seismic anisotropy stays at about to AVp = 8.2% for the strain of 0.5 and increases up to AVp = 17.4% at strain of 2.

4. Discussion

4.1. Texture Evolution in Uniaxial Deformation Experiments

The interpretation of seismic anisotropy relies on our understanding of the way crystals rotate and align in a polycrystalline aggregate under externally imposed deformation conditions. *Nicolas et al.* [1973] were the first to demonstrate how texture in olivine develops and strengthens as a function of strain in uniaxial compression. In these experiments, a CPO develops in which the [010] axes align parallel to the direction of compression and the [100] and [001] axes align within the radial plane, perpendicular to the compression axis. Put in terms of P, G, and R, the *Nicolas et al.* [1973] experiments predict that olivine in uniaxial compression should accumulate a strong G$_{[100]}$, P$_{[010]}$, and G$_{[001]}$, with a corresponding decrease in the R component of all three pole figures. For several decades, these experiments have provided an important basis for modeling and interpreting CPO and anisotropy in mantle rocks [e.g., *Karato et al.*, 2008].

Building on the *Nicolas et al.* [1973] experiments, *Boneh and Skemer* [2014] showed the effect of deformation history on texture evolution in uniaxial compression. Unlike the *Nicolas et al.*, 1973 experiments, which used samples with a weak preexisting CPO, Boneh and Skemer conducted experiments on the Åheim dunite, which possesses a strong preexisting texture. Experiments were conducted in three different configurations to simulate distinct deformation histories. As with the Nicolas et al. experiments,
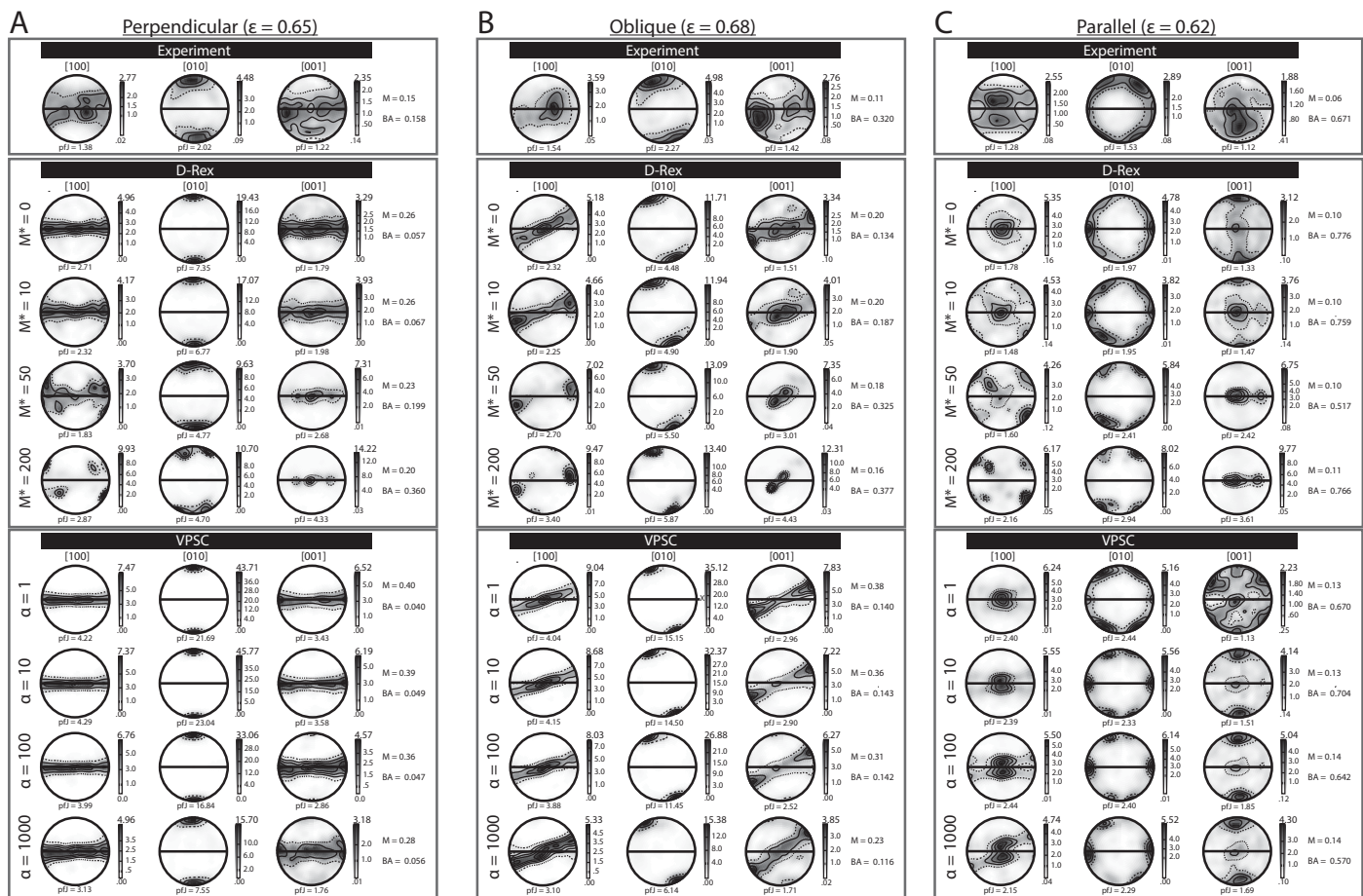
Figure 5. Pole figures showing texture from experiments (top row), D-Rex (second through fifth rows), and VPSC (six through ninth rows) for the three starting configurations: (a) perpendicular, (b) oblique, and (c) parallel. Models are shown for a range of parameters: for D-Rex, M* = 0, 10, 50 or 200, and for VPSC α = 1, 10, 100, or 1000. Experimental data are taken from high strain experiments of *Boneh and Skemer* [2014], and is the same as Figure 2. Scale bar to the right of each pole figure show the multiples of uniform distribution (m.u.d.). Pole figures projected in equal area and lower hemisphere. Texture strength of each pole figure (pfJ), the total texture strength (M-index) and texture symmetry (BA-index) are given.

Boneh and Skemer [2014] showed that texture evolves toward a symmetry characterized by strong point maxima in [010] and girdles in the [100] and [001] pole figures. However, for strains of $\sim$ 0.6–0.7, texture evolution is still transient, and is far from the expected steady state, particularly in the oblique and parallel cases (Figure 2). Moreover, each experimental configuration evolved differently as a function of strain. Here we demonstrate that numerical models of texture evolution, run using identical starting conditions, lead to the same conclusions: that deformation history significantly influences the way texture accumulates with progressive strain (Figures 2–4).

4.2. Comparison Between Numerical Models and Experiments

In general, comparison between numerical models and experiments reveals a similar texture signature but with significant differences in the CPO strength and the magnitude of the calculated anisotropy (Figures 2 and 4). For the three configurations, models show the development of a [010] point maximum parallel to the shortening axis, in excellent agreement with the experiments (see further discussion in section 4.4). For the [100] and [001] axes there are some differences between the two models and the experiments (especially in the oblique and parallel configurations). For example, in the oblique configuration, D-Rex shows [100] and [001] point maximum near the X and Y directions, respectively while VPSC shows [100] and [001] point maximum near the Y and X directions, respectively (Figure 2). In nearly all cases, the VPSC and D-Rex models overestimate the strength of the CPO, and therefore the magnitude of the seismic anisotropy.

With both the VPSC and the D-Rex models, parameterization is achieved mainly through comparison with laboratory experiments. The experimental benchmarks for the D-Rex models of *Kaminski et al.* [2004] and

the VPSC models of *Tommasi et al.* [2000] are the experiments of *Zhang and Karato* [1995] and *Nicolas et al.* [1973]. Both of these studies used olivine aggregates with near-random initial CPO. Hence, models parameterized through comparison with these experiments are not optimized to account for the effects of preexisting texture, which should be ubiquitous in the upper mantle. In this study we have explored a range of model parameter space to determine those that best simulate CPO evolution in more complex geologic scenarios (Figure 5).

As noted earlier, D-Rex includes three nondimensional parameters that influence model results—M^*, λ^* and χ. We tested a range of values for each parameter ($M^* = 0$–200, $\lambda^* = 0$–5, and $\chi = 0$–0.8) and found that the M^* parameter has the most pronounced effect on the resulting texture while λ^*, and χ parameters have a relatively small influence that becomes negligible when recrystallization and recovery processes are slow (i.e., at low M^* values). Therefore, we use common values for grain nucleation and grain boundary sliding threshold: $\lambda^* = 5$ and $\chi = 0.3$ [*Kaminski and Ribe*, 2001; *Kaminski et al.*, 2004] throughout the present study, and focus on the effect of parameter M^* on texture.

Figure 5 shows model results for M^* values of: 0, 10, 50, and 200. *Kaminski and Ribe* [2001] showed that M^* between 50 and 200 fits textures from past experiments [*Nicolas et al.*, 1973; *Zhang and Karato*, 1995] with larger values favored at higher temperatures when grain-boundary migration is more efficient. However, larger values of M^* appear to erase preexisting texture efficiently or generate unexpected textures that are inconsistent with experimental results. Grain boundary migration (M^*) causes each grain to grow or shrink according to whether its strain energy is higher or lower than the average strain energy [*Kaminski and Ribe*, 2001, equation (14)]. The rate of new grain nucleation (λ^*) increases with higher ratio of dislocation density (equation (4)). Modeling both processes enhances texture evolution: grain nucleation produces a large volume fraction of strain-free nucleated grains that have the largest growth rate as they have the smallest strain energy compared to the average strain energy of the aggregate. Because the growth rate is proportional to both the difference in strain energy and the grain boundary mobility (M^*), the larger M^* the larger the growth rate of nucleated strain-free grains in soft orientations. For example, in Figure 5a we show CPOs generated in the perpendicular configuration. Experiments in this configuration produce an AG-type CPO with axial girdles in the [100] pole figures. However in models for which M^* is large (50 and 200) the girdle is largely obscured by clusters of orientations that fall outside of the axial plane. Likewise, in Figure 5b, we see for $M^* = 50$ and 200 an elimination of the preexisting [100] girdle and the development of point maxima that are nearly perpendicular to the experimental observation. Based on comparison with the *Boneh and Skemer* [2014] experiments we suggest that lower values of M^* (i.e., $M^* = 10$) may be more appropriate for modeling CPO evolution influenced by preexisting texture. Although not considered here, future efforts may also benefit from implementation of D-Rex parameters that depend on both deformation mechanism and deformation history.

Using the VPSC model, we generate CPO pole figures with α values of 1, 10, 100, and 1000 (Figure 5). The α parameter simulates grains interactions between two end members: when grains experience equal strain ($\alpha = 0$) and when grains experience equal stress (α approaches infinity). The most commonly used values for α are $\alpha = 1$, which is the tangent VPSC model [*Lebensohn and Tomé*, 1993; *Molinari et al.*, 1987], and $\alpha = 10$–100, which assumes some relaxed strain compatibility [*Tommasi et al.*, 2000]. In Figure 5, we compare models for $\alpha = 1$–1000. We find that α affects mainly the strength of the CPO and has only minor effect on the symmetry. The best fit with the experimental data is found to be $\alpha = 10$–100. In the remainder of this study we chose to use $\alpha = 100$.

4.3. The Role of Dynamic Recrystallization and Secondary Deformation Mechanisms

Dynamic recrystallization by both subgrain rotation and grain boundary migration is expected and observed in experiments and nature. One of the main differences between the two numerical models is that D-Rex simulates the effects of dynamic recrystallization by nucleation and growth, while in our version of the VPSC model dynamic recrystallization is not modeled. Dynamic recrystallization in D-Rex is simulated by two processes, grain nucleation and grain boundary migration. The activity of these two recrystallization processes is controlled by the dislocation density. The effect of dynamic recrystallization is to increase the volume fraction of strain-free newly nucleated grains with a soft orientation relative to the imposed deformation. An example of the effect of dynamic recrystallization on texture can be seen in the [001] axis of the parallel configuration (Figure 2c). For both models, there are two groups of grains that can be clearly seen

as different maxima parallel to the Y and the Z axes. The first fraction of grains with [001] parallel to Z axis, have [100] orientated parallel to Y axis, and [010] parallel to X axis. This set of grains experience minimal rotation and have stayed approximately at their original orientation. The second fraction of grains with [001] oriented parallel to Y axis, have [100] oriented in an "x" shape (D-Rex) or along the X-Y plane (VPSC), and [010] along the X-Z plane. These grains represent the population of grains that experienced significant reorientation. In D-Rex the two populations of grains represent a similar volume fraction of the aggregate while in VPSC the first fraction of grains (which represents grains with no rotation) is significantly larger than the second fraction of grains (which represents rotated grains). The experimental data show a dispersed [001] with a maximum around Y axis with no apparent point maxima parallel to the X axis. We interpret this observation to indicate that the pole figures from experiments contain very few grains from the fraction of relict orientations that experienced minimal rotation. Eliminating the extra [001] point maxima in D-Rex can be achieved by using a higher value for grain boundary mobility (M^*) although that will modify other aspects of texture and will yield a less ideal fit with the experiments.

A further element of D-Rex is a grain size threshold (χ) that simulates the activity of other deformation mechanisms such as diffusion creep and/or grain boundary sliding (GBS). This is implemented in a way that disables the rotation of small grains, hence decreasing the rate of evolution of the CPO when grain-size is reduced. Although the influence of diffusion creep and GBS on CPO evolution is complex [e.g., *Wheeler*, 2009], several observations have asserted that GBS acts to disperse texture [*Skemer and Karato*, 2008; *Warren and Hirth*, 2006]. The high CPO strength in D-Rex, compared to experiments (Figure 4a), suggests that an additional CPO weakening process for simulating GBS or diffusion creep mechanisms may be needed. Interestingly, although the pervasive recrystallization is observed in the samples from *Boneh and Skemer* [2014], the orientation and symmetry of the CPO simulated by VPSC is in good agreement with the experimental CPO (Figure 2). This suggests that under some conditions grain size reduction via dynamic recrystallization causes a general CPO dispersion, weakening the texture but not significantly altering its symmetry or orientation.

Future versions of texture models may benefit from subroutines that progressively randomize texture when grain-size is reduced below a certain threshold and indeed there have been a number of recent advances in the simulation of dynamic recrystallization processes (e.g., the CDRX-VPSC model of *Signorelli and Tommasi* [2015]. Validation of new models will benefit from additional comparisons between existing models, such as the work by *Castelnau et al*. [2008], and comparisons with experimental results such as *Boneh and Skemer* [2014], applying the more stringent requirement that models must be able to reproduce a full spectrum of deformation histories.

4.4. Development of Orthorhombic Textures: Transient or Steady State?

Under uniaxial deformation conditions, steady state CPO should be characterized by radial girdles of [100] and [001] axes and a point maximum in the [010] axis [*Nicolas et al*., 1973; *Wenk et al*., 1991]. Girdles are expected in the [100] and [001] pole figures because under these imposed deformation conditions there is no preferred kinematic direction in the X-Y plane. Interestingly, *Boneh and Skemer* [2014] observed the development of an unexpected asymmetry in this texture: a point maximum in the [100] axis along the Y axis (parallel to the strike of the foliation in the sample reference frame). In both VPSC and D-Rex models, the development of this point maxima is not observed when an initial random texture is used (gray symbols in Figures 6a–6c). However, in simulations initiated with a nonrandom texture, both VPSC and D-Rex predict a very dominant point maxima parallel to Y, in agreement with the experimental results. This is particularly apparent in the oblique and parallel configurations (Figures 6b and 6c).

For the oblique and parallel cases, this quasi-orthorhombic texture under axial deformation can be explained when considering the influence of the preexisting girdled texture. The [100] and [001] girdles in the Åheim dunite, in the oblique and parallel configurations, are in unstable positions with respect to the imposed deformation. However, within this girdle, a fraction of the grains have their [100] axes oriented along the foliation strike (Y axis). These grains, with the [100] axis already oriented parallel to the Y axis, do not need to rotate in order to align toward the X-Y plane; other grains with [100] axes oblique to the X-Y plane require some rotation to reach the steady state orientation. Rotated grains are dispersed while the grains that do not rotate become a point maxima in the axis of rotation (Y axis). This produces a transient pseudo-orthorhombic symmetry to the CPO.
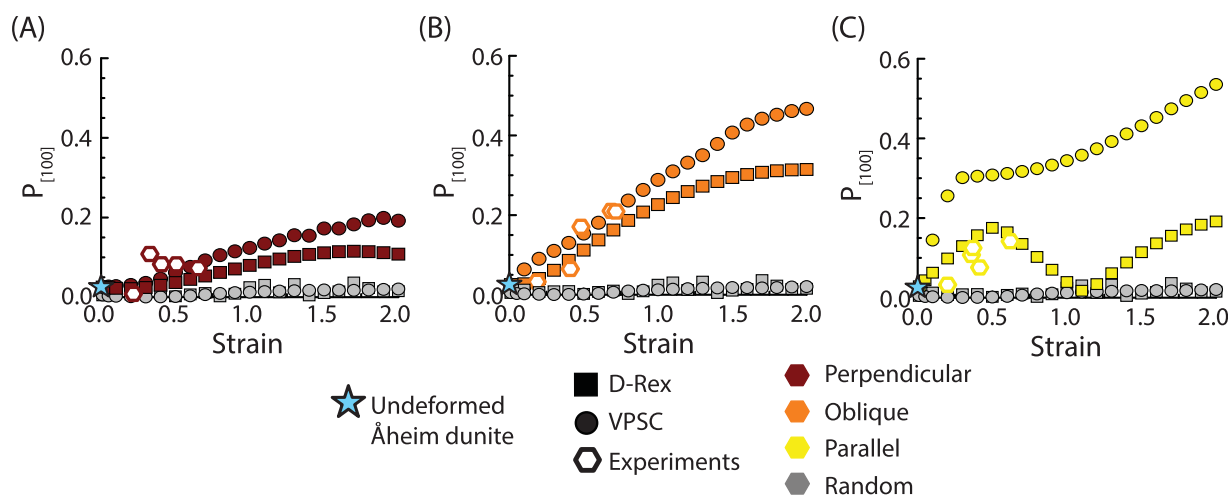
Figure 6. The $P_{[100]}$ parameter is plotted versus strain for the three configurations: dark red for (a) perpendicular, (b) orange for oblique, and (c) yellow for parallel for D-Rex (squares), VPSC (circles) and experiments (open symbols). For reference, models initiated with a random texture are shown in gray (these results are the same in Figures 6a–6c). Blue stars denote the initial $P_{[100]}$ of the undeformed Åheim dunite. Numerical models initiated with random textures do not display any perceptible increase in $P_{[100]}$ with strain. However models and experiments initiated using the preexisting texture show a systematic increase of $P_{[100]}$ with strain, reflecting the generation and strengthening of CPOs with orthorhombic symmetries .

For the perpendicular case, experiments and models are initiated with strong [100] and [001] girdles already oriented in accordance with the imposed deformation kinematics. Interestingly, a [100] point maxima still develops with strain, both for D-Rex and VPSC (Figure 6a), although this behavior is not seen in models initiated with a random texture, which develop an almost ideal girdle in [100] (gray symbols in Figures 3a and 3b). A likely explanation is that the Åheim dunite does not have a perfect girdle to begin with and that the observed point maxima in models is a consequence of small initial perturbations in the natural CPO (Figure 1a), which are enhanced with strain.

A critical question from the perspective of understanding CPO in the mantle is whether these textures are transient or steady state. If these textures are transient, how long are the transient CPOs maintained? If unexpected CPOs are preserved over long strain intervals this significantly changes the approach that must be used when interpreting seismic anisotropy in terms of mantle flow. To evaluate this, we look at how texture quantities vary as a function of strain. One way to quantify a coaxial texture, with a girdle in the [100] pole figure and a point maximum in the [010] pole figure, is through the BA-index defined in equation (6) [*Mainprice et al.*, 2014]. Figure 7 shows the BA-index development with strain for D-Rex and VPSC for the three different configurations with preexisting texture and for an initial random texture. The models with an initial random texture exhibit a rapid decrease of the BA-index to extremely low, and apparently steady state values (BA = 0.01–0.03 and 0.01–0.02 for D-Rex and VPSC, respectively). The strain required to reach this steady state value is minimal ($\varepsilon \sim 0.2$–0.3). This observation would imply that evolution of CPO is rapid and predictable. The pretextured configurations also appear to reach a steady BA value however the strain required to reach this apparent steady state value is considerably larger, especially in the parallel configuration. Moreover, the magnitude in each configuration is significantly different (BA perpendicular > BA oblique > BA parallel > 0 for both models). The fact that the BA value of different configurations do not converge to zero illustrates the protracted effect of the initial texture on the ultimate steady state. Models up to strains of 2 do not eliminate the inherited point maximum, and perhaps achieve a quasi-steady state CPO that depends on the initial model conditions. Tests using D-Rex up to strains of $\varepsilon = 10$ observe no additional change in this observation.

4.5. Seismic Anisotropy Resulting From Transient CPO Evolution
At the conditions prevalent in the upper mantle, convection driven flow at large or small scales will generate CPO as a natural consequence of deformation [*Karato et al.*, 2008]. Near plate boundaries, where deformation conditions and kinematics change rapidly, progressive deformation will continuously overprint a long and complex convective history. If texture evolution is slow in comparison to these changes, seismic anisotropy will reflect the transient nature of the CPO [*Kaminski and Ribe*, 2002; *Lassak et al.*, 2006]. Seismic
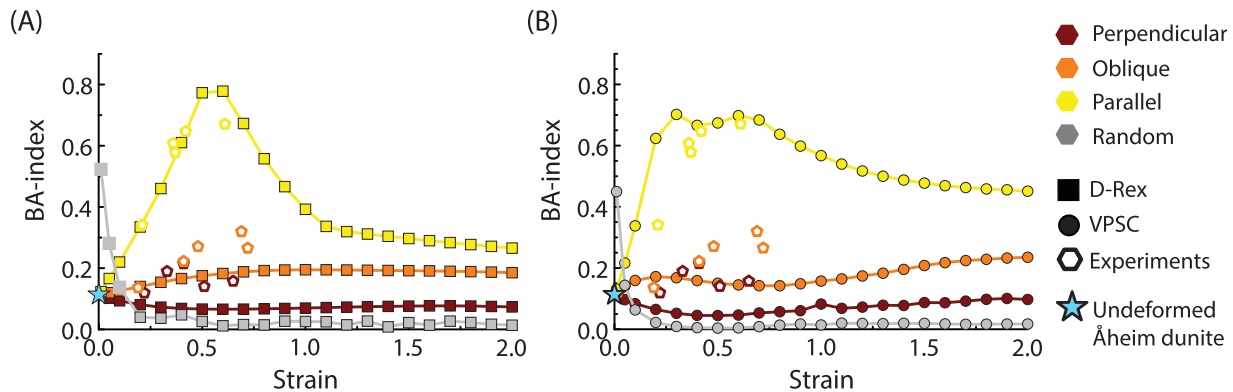
Figure 7. The BA-index is plotted versus strain for (a) D-Rex and (b) VPSC for the three configurations: perpendicular in dark red, oblique in orange, and parallel in yellow. Models initiated with a random texture are shown in gray. Blue stars denote the initial $P_{[100]}$ of the undeformed Åheim dunite. Models initiated with a random texture converge rapidly to BA $\sim$ 0, indicating that the CPO achieves a nearly perfect axial girdle (AG). All of the pretextured configurations appear to stabilize at some nonzero BA-index, reflecting deviations from the idealized texture. There is no convergence of BA values at high strain, indicating that deformation history influences CPO symmetry over long transient strain intervals.

anisotropy detects CPO strength, symmetry, and orientation but is primarily sensitive to the latter two characteristics.

The numerical simulations presented in section 3.2 emphasize that the details of the deformation history affect significantly the consequent CPO (Figure 3). In Figures 8a-8c, we show how these CPOs manifest as different seismic signatures. In Figures 8d and 8e, we show for comparison the calculated seismic
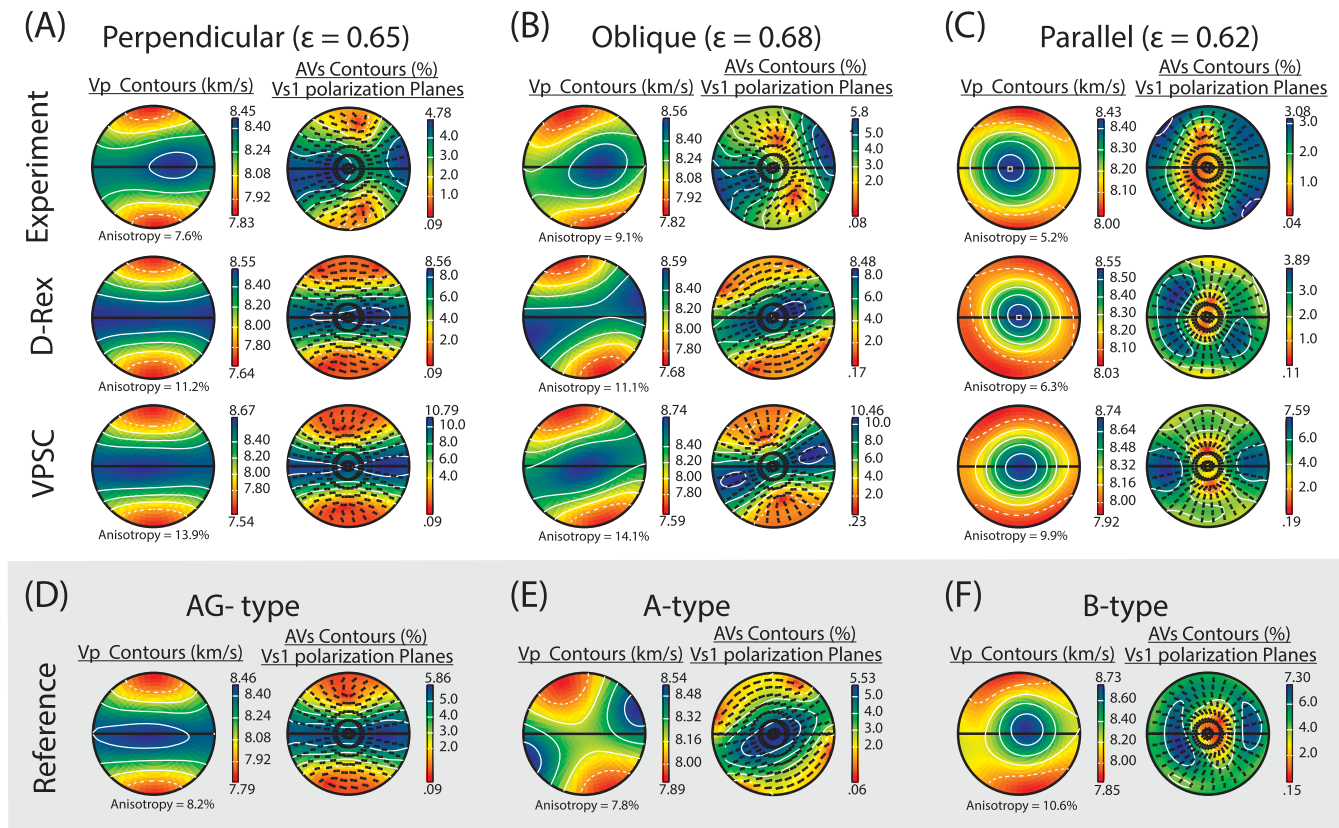

Figure 8. Pole figures showing anisotropic seismic properties calculated from textures of experiments and models projected in the lower hemisphere. Three seismic properties are shown for each model or sample: (left) Vp (km/s), (right) AVs (%) (AVs = 200 (Vs$_{max}$−Vs$_{min}$)/(Vs$_{max}$ + Vs$_{min}$), color, and the polarization, vector, of the fast shear waves. Color contours ranges from red (low velocities) to blue (high velocities). We show experiments and models for the three sample configurations: (a) perpendicular, (b) oblique, and (c) parallel. Seismic anisotropy calculated for experiments and models are compared at the same strain, as in Figure 2. Several reference samples to be compared with the present study: (d) an AG-type fabric, represented by undeformed Åheim dunite, (e) an A-type fabric (sample PI-284) from the experiments of *Zhang et al.* [2000] deformed experimentally under anhydrous conditions in simple shear, and (f) a B-type fabric (sample JK-21), deformed experimentally by [*Jung and Karato*, 2001] under hydrous conditions in simple shear.
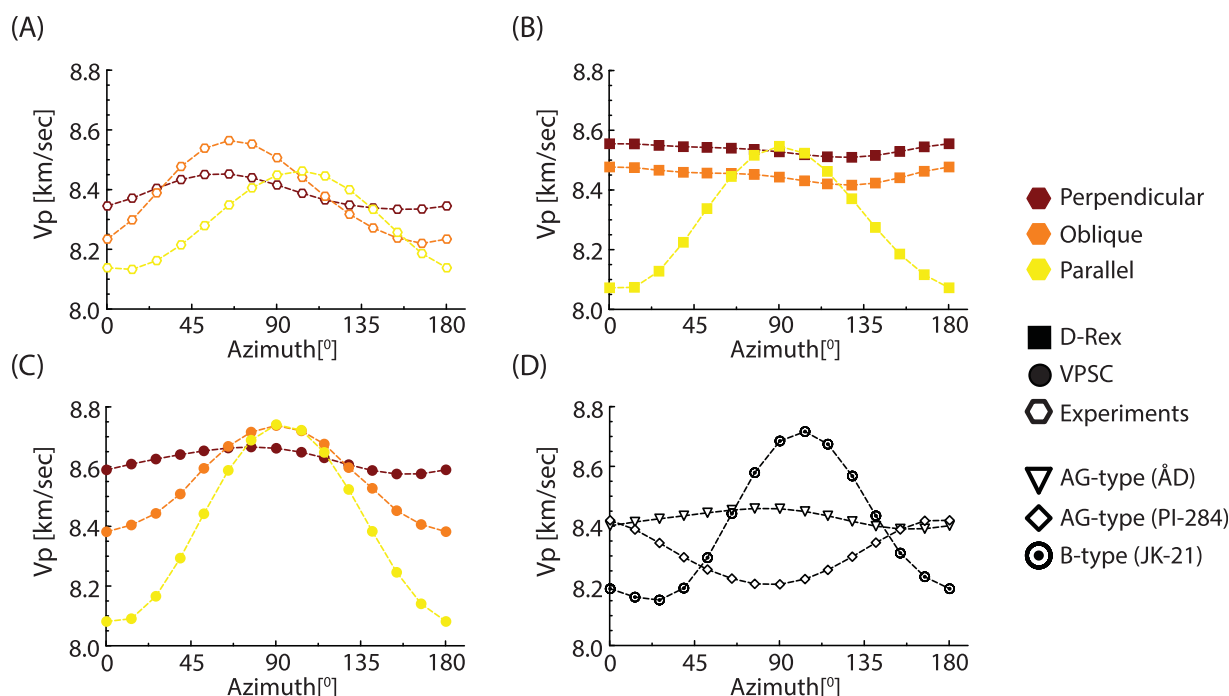
Figure 9. P-wave velocity is plotted against azimuthal angle (in degrees) along the radial X-Y plane. 0 and 180° correspond to the sample X direction; 90° corresponds to the sample Y direction. Vp variation with respect to the azimuth angles is shown for perpendicular (dark red), oblique (orange), and parallel (yellow) configurations, in (a) experiments (hollow symbols), (b) D-Rex (square symbols), and (c) VPSC (circle symbols), respectively. (d) Variation of Vp with azimuth is calculated for the three reference textures shown in Figure 8D, 8E, and 8F. Samples with well-developed axial girdles exhibit the lowest azimuthal anisotropy. However many samples, especially those deformed in the parallel configuration, exhibit significant anisotropy. The anisotropy of the samples in the parallel and oblique configurations have anisotropy signatures that are very similar to the B-type reference sample, although the CPOs were generated under very different conditions.

anisotropy for three other common CPOs. This illustrates how different deformation histories may yield similar anisotropies—note for example, the similarity between the anisotropy generated in the parallel configuration and the anisotropy generated by a "B-type" fabric. Experiments and models are generally in agreement although the models over-predict the magnitude of anisotropy, in some cases by a factor of two. Experiments and models in the perpendicular configuration show the strongest agreement, which is to be expected because there is assumed to be no change in deformation kinematics between the preexisting deformation and imposed deformation stages. Data for the parallel configuration are also in excellent agreement. The anisotropy in this configuration is quite distinct from the predicted steady state anisotropy, with a strong P-wave velocity maximum parallel to the Y direction (see section 4.4). The oblique configuration shows the greatest difference between the experiment and the models. The fastest P-wave direction in the VPSC and in the experimental data is roughly parallel to the Y direction, as is also seen in the parallel configuration. However in the D-Rex model the fastest P-wave direction is subparallel to the X axis (Figure 8b). Hence the two models predict anisotropy that is roughly orthogonal. In general, all three deformation or simulation configurations predict distinct seismic signatures. In Figure 9, P-wave velocities are shown with respect to the azimuth angle along the plane normal to the shortening axis (X-Y plane) for experiments, D-Rex, and VPSC (Figures 9a–9c, respectively). The P-wave velocities vary significantly depending on the direction of wave propagation for the oblique (experiments and VPSC) and parallel (experiments, D-Rex, and VPSC) data sets, reflecting the relict textures.

When CPO symmetries are orthorhombic (and hence do not exhibit transverse isotropy) a maximum in P-wave velocity along a specific radial azimuth is expected. This P-wave velocity maximum should be parallel to the X direction in A-type fabric and parallel to the Y direction for B-type fabric [*Jung and Karato*, 2001]. Although both models and experiments have the same dominant slip system as the AG-type CPOs regardless of the initial configuration, transient texture development produces seismic anisotropy that may be similar signature to orthorhombic A-type or B-type textures. That suggests that the relationship between seismic anisotropies and mantle flow is nonunique in regimes where a transient stage of texture evolution is expected.
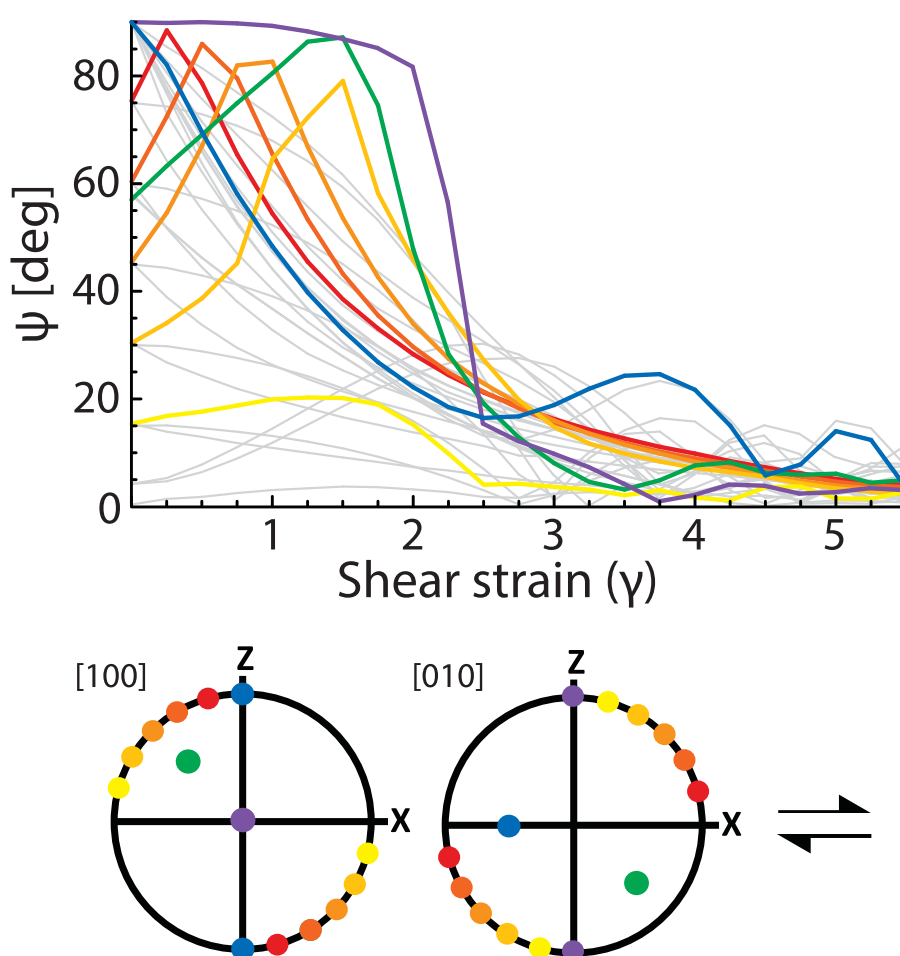
Figure 10. Simple shear simulations generated using the D-Rex model (M* = 10) for a range of initial orientations. To represent the first stage of deformation, a strong orthorhombic texture (M = 0.31) was rotated into 33 different orientations, mostly along the XY, XZ, and YZ planes. A second stage of deformation was then imposed, up to $\gamma = 5.5$. CPO evolution is described by the angle of rotation, ψ, which is defined as the smallest angle between the [100] point maxima and the X direction (i.e., $0 < \psi < 90$). The curves show the evolution of ψ with respect to shear strain (γ), for each of the starting orientations. Of the 33 simulations, 25 are shown in gray to illustrate the range of possible orientations that might be expected given a large number of starting configurations. 8 representative simulations are shown in colors corresponding to specific initial configurations (shown in the key). Curves in yellow-orange-red reflect the scenario where a sample is sheared first with one shear sense, and then the opposite shear sense, along similar shear planes-a plausible scenario as material is advected through the mantle wedge. Collectively, these curves document a long transient stage ($\gamma = 0$ to ~4) where there is significant variability in CPO orientation, and a subsequent stage ($\gamma > 4$) where CPOs reach a quasi-steady state and the obliquity between the CPO and the flow direction is smaller and generally predictable.

4.6. Simple Shear Deformation

In many plate boundary settings deformation is likely to include elements of both simple and pure shear [*Tommasi et al.*, 1999]. Indeed, recent models of mantle flow around subducting slab show that compressional or tensional coaxial deformation, due slab roll back and three dimensional flow, could be the dominant deformation geometry in these settings [*Di Leo et al.*, 2014; *Faccenda and Capitanio*, 2013; *Kneller and van Keken*, 2007; *Long and Silver*, 2009]. To permit direct comparison between experiments and models, the present study focused on deformation with a uniaxial shortening geometry. However, to extend the results of this study to more general scenarios we have conducted some additional simulations of CPO evolution in simple shear.

Evolution of CPO in simple shear is illustrated through the rotation of the [100] maxima (approximating the fast seismic direction) as a function of strain (Figure 10). The [100] maxima orientation, ψ, is defined here as the angle between the point maxima (i.e., the orientation of the largest eigenvalue) and the X direction. For these simulations a strong (M = 0.31) orthorhombic A-type CPO was created using D-Rex, with the [100] axes aligned parallel to the shear direction (X axis). This CPO was rotated, mainly along the XY, XZ, and YZ

planes, for a total of 33 different initial orientations. This assortment of initial textures was then deformed in simple shear to a maximum strain of $\gamma = 5.5$ (Figure 10). Due to the large strains required for these simulations, we show results only for the D-Rex model. The collection of curves shows two stages. At low to moderate strains CPO evolution is transient, with the [100] orientation are distributed broadly in orientation space. Most models exhibit a [100] maxima that is highly oblique to the shear direction, and there is significant variation amongst the different simulations. The second stage of evolution occurs at larger strains ($\gamma > 4$), in which a quasi-steady state is reached, and the [100] maximum is generally within 0–10° of the shear direction. Notably, the critical strains required to reset preexisting CPO are quite consistent with observations from natural samples [*Skemer et al.*, 2012; *Warren et al.*, 2008].

5. Conclusions

In this study, D-Rex and VPSC models are used to evaluate texture evolution of olivine aggregates for a variety of initial conditions, simulating distinct deformation histories. These models were compared with recent experiments by *Boneh and Skemer* [2014]. Both experiments and numerical models show that deformation history has a significant impact on the evolution of olivine CPO. For each of the initial deformation configurations, CPO and the consequent anisotropic signature is observed to evolve differently. Moreover, the evolution of CPO in each deformation configuration deviates markedly from the evolution of experiments and models initiated with random textures. In a uniaxial deformation geometry to strains of $\varepsilon = 2$, models in various configurations do not converge to the predicted steady state texture. Models run to larger strains in simple shear, appear to converge to steady state textures at $\gamma > 3$. This is significantly larger than previously assumed, but is largely consistent with observations from mantle shear zones. It should also be noted that these critical strains for reorientation are similar in magnitude to strains generated by corner-flow in a subduction setting [e.g., *McKenzie*, 1979]. As such, forward or inverse models that seek to relate seismic anisotropy to mantle flow must be cautious in their interpretations, as olivine appears to exhibit long transient intervals during which CPO has not reached steady state.

References

Abramson, E. H., M. Brown, L. J. Slutsky, and J. Zaug (1997), The elastic constants of San Carlos olivine up to 17 GPa, *J. Geophys. Res.*, *102*, 12,252-12,263.

Alpert, L. A., M. S. Miller, T. W. Becker, and A. A. Allam (2013), Structure beneath the Alboran from geodynamic flow models and seismic anisotropy, *J. Geophys. Res. Solid Earth*, *118*, 4265–4277, doi:10.1002/jgrb.50309.

Ave Lallemant, H. (1975), Mechanisms of preferred orientations of olivine in tectonite peridotite, *Geology*, *3*, 653.

Bachmann, F., R. Hielscher, and H. Schaeben (2010), Texture analysis with MTEX–free and open source software toolbox, *Solid State Phenomena*, *160*, 63–68, doi:10.4028/www.scientific.net/SSP.160.63.

Bai, Q., S. J. Mackwell, and D. L. Kohlstedt (1991), High-temperature creep of olivine single crystals 1. Mechanical results for buffered samples, *J. Geophys. Res.*, *96*, 2441–2463, doi:10.1029/90JB01723.

Becker, T. W., S. Chevrot, V. Schulte-Pelkum, and D. K. Blackman (2006a), Statistical properties of seismic anisotropy predicted by upper mantle geodynamic models, *J. Geophys. Res.*, *111*, B08309, doi:10.1029/2005JB004095.

Becker, T. W., V. Schulte-Pelkum, D. K. Blackman, J. B. Kellogg, and R. J. O'Connell (2006b), Mantle flow under the western United States from shear wave splitting, *Earth Planet. Sci. Lett.*, *247*(3–4), 235–251, doi:10.1016/j.epsl.2006.05.010.

Becker, T. W., C. P. Conrad, A. J. Schaeffer, and S. Lebedev (2014), Origin of azimuthal seismic anisotropy in oceanic plates and mantle, *Earth Planet. Sci. Lett.*, *401*, 236–250, doi:10.1016/j.epsl.2014.06.014.

Ben Ismaïl, W., and D. Mainprice (1998), An olivine fabric database: An overview of upper mantle fabrics and seismic anisotropy, *Tectonophysics*, *296*, 145–157, doi:10.1016/S0040-1951(98)00141-3.

Blackman, D. (2007), Use of mineral physics, with geodynamic modelling and seismology, to investigate flow in the Earth's mantle, *Rep. Prog. Phys.*, *70*(5), 659.

Blackman, D. K., and J. M. Kendall (2002), Seismic anisotropy in the upper mantle 2. Predictions for current plate boundary flow models, *Geochem. Geophys. Geosyst.*, *3*(9), 8602, doi:10.1029/2001GC000247.

Blackman, D. K., J. Kendall, P. R. Dawson, H. Wenk, D. Boyce, and J. P. Morgan (1996), Teleseismic imaging of subaxial flow at mid-ocean ridges: Traveltime effects of anisotropic mineral texture in the mantle, *Geophys. J. Int.*, *127*(2), 415–426, doi:10.1111/j.1365-246X.1996.tb04730.x.

Boneh, Y., and P. Skemer (2014), The effect of deformation history on the evolution of olivine CPO, *Earth Planet. Sci. Lett.*, *406*, 213–222, doi:10.1016/j.epsl.2014.09.018.

Bonnin, M., A. Tommasi, R. Hassani, S. Chevrot, J. Wookey, and G. Barruol (2012), Numerical modelling of the upper-mantle anisotropy beneath a migrating strike-slip plate boundary: The San Andreas Fault system, *Geophys. J. Int.*, *191*(2), 436–458, doi:10.1111/j.1365-246X.2012.05650.x.

Castañeda, P. P. (2002), Second-order homogenization estimates for nonlinear composites incorporating field fluctuations: I—Theory, *J. Mech. Phys. Solids*, *50*(4), 737–757, doi:10.1016/S0022-5096(01)00099-0.

Castelnau, O., R. Brenner, and R. Lebensohn (2006), The effect of strain heterogeneity on the work hardening of polycrystals predicted by mean-field approaches, *Acta Materialia*, *54*(10), 2745–2756, doi:10.1016/j.actamat.2006.02.014.

Castelnau, O., D. Blackman, R. Lebensohn, and P. Ponte Castañeda (2008), Micromechanical modeling of the viscoplastic behavior of olivine, *J. Geophys. Res.*, *113*, B09202, doi:10.1029/2007JB005444.

Castelnau, O., D. Blackman, and T. Becker (2009), Numerical simulations of texture development and associated rheological anisotropy in regions of complex mantle flow, *Geophys. Res. Lett.*, *36*, L12304, doi:10.1029/2009GL038027.

Castelnau, O., P. Cordier, R. Lebensohn, S. Merkel, and P. Raterron (2010), Microstructures and rheology of the Earth's upper mantle inferred from a multiscale approach, *C. R. Phys.*, *11*(3), 304–315, doi:10.1016/j.crhy.2010.07.011.

Chastel, Y. B., P. R. Dawson, H. R. Wenk, and K. Bennett (1993), Anisotropic convection with implications for the upper mantle, *J. Geophys. Res.*, *98*, 17,757-17,771.

Chopra, P. N., and M. S. Paterson (1981), The experimental deformation of dunite, *Tectonophysics*, *78*, 453–473, doi:10.1016/0040-1951(81)90024-X.

Chopra, P. N., and M. S. Paterson (1984), The role of water in the deformation of dunite, *J. Geophys. Res.*, *89*, 7861–7876.

Conder, J. A., and D. A. Wiens (2007), Rapid mantle flow beneath the Tonga volcanic arc, *Earth Planet. Sci. Lett.*, *264*(1), 299–307, doi: 10.1016/j.epsl.2007.10.014.

Conrad, C. P., M. D. Behn, and P. G. Silver (2007), Global mantle flow and the development of seismic anisotropy: Differences between the oceanic and continental upper mantle, *J. Geophys. Res.*, *112*, B07317, doi:10.1029/2006JB004608.

Detrez, F., O. Castelnau, P. Cordier, S. Merkel, and P. Raterron (2015), Effective viscoplastic behavior of polycrystalline aggregates lacking four independent slip systems inferred from homogenization methods; application to olivine, *J. Mech. Phys. Solids*, *83*, 199–220, doi: 10.1016/j.jmps.2015.05.022.

Di Leo, J., A. Walker, Z. H. Li, J. Wookey, N. Ribe, J. M. Kendall, and A. Tommasi (2014), Development of texture and seismic anisotropy during the onset of subduction, *Geochem. Geophys. Geosyst.*, *15*, 192–212, doi:10.1002/2013GC005032.

Druken, K., M. Long, and C. Kincaid (2011), Patterns in seismic anisotropy driven by rollback subduction beneath the High Lava Plains, *Geophys. Res. Lett.*, *38*, L13310, doi:10.1029/2011GL047541.

Druken, K., C. Kincaid, and R. Griffiths (2013), Directions of seismic anisotropy in laboratory models of mantle plumes, *Geophys. Res. Lett.*, *40*, 3544–3549, doi:10.1002/grl.50671.

Durham, W. B., and C. Goetze (1977), Plastic flow of oriented single crystals of olivine 1. Mechanical data, *J. Geophys. Res.*, *82*, 5737–5753.

Eshelby, J. D. (1957), The determination of the elastic field of an ellipsoidal inclusion, and related problems, in *Proceedings of the Royal Society of London A: Mathematical, Physical and Engineering Sciences*, *241*(1226), 376–396.

Faccenda, M., and F. Capitanio (2013), Seismic anisotropy around subduction zones: Insights from three-dimensional modeling of upper mantle deformation and SKS splitting calculations, *Geochem. Geophys. Geosyst.*, *14*, 243–262, doi:10.1002/ggge.20055.

Faccenda, M., and F. A. Capitanio (2012), Development of mantle seismic anisotropy during subduction-induced 3-D flow, *Geophys. Res. Lett.*, *39*, L11305, doi:10.1029/2012GL051988.

Falus, G., A. Tommasi, and V. Soustelle (2011), The effect of dynamic recrystallization on olivine crystal preferred orientations in mantle xenoliths deformed under varied stress conditions, *J. Struct. Geol.*, *33*(11), 1528–1540, doi:10.1016/j.jsg.2011.09.010.

Hansen, L. N., M. E. Zimmerman, and D. L. Kohlstedt (2012), Laboratory measurements of the viscous anisotropy of olivine aggregates, *Nature*, *492*(7429), 415–418, doi:10.1038/nature11671.

Hansen, L. N., Y.-H. Zhao, M. E. Zimmerman, and D. L. Kohlstedt (2014), Protracted fabric evolution in olivine: Implications for the relationship among strain, crystallographic fabric, and seismic anisotropy, *Earth Planet. Sci. Lett.*, *387*, 157–168, doi:10.1016/j.epsl.2013.11.009.

Hedjazian, N., and E. Kaminski (2014), Defining a proxy for the interpretation of seismic anisotropy in non-Newtonian mantle flows, *Geophys. Res. Lett.*, *41*, 7065–7072, doi:10.1002/2014GL061372.

Higgie, K., and A. Tommasi (2012), Feedbacks between deformation and melt distribution in the crust–mantle transition zone of the Oman ophiolite, *Earth Planet. Sci. Lett.*, *359*, 61–72, doi:10.1016/j.epsl.2012.10.003.

Jackson, I., M. Paterson, and J. Fitz Gerald (1992), Seismic wave dispersion and attenuation in Åheim dunite: An experimental study, *Geophys. J. Int.*, *108*(2), 517–534, doi:10.1111/j.1365-246X.1992.tb04633.x.

Jung, H., and S.-i. Karato (2001), Water-induced fabric transitions in olivine, *Science*, *293*, 1460–1463, doi:10.1126/science.1062235.

Kaminski, É., and N. M. Ribe (2001), A kinematic model for recrystallization and texture development in olivine polycrystals, *Earth Planet. Sci. Lett.*, *189*(3–4), 253–267, doi:10.1016/S0012-821X(01)00356-9.

Kaminski, É., and N. M. Ribe (2002), Timescales for the evolution of seismic anisotropy in mantle flow, *Geochem. Geophys. Geosyst.*, *3*(8), 1051, doi:10.1029/2001GC000222.

Kaminski, É., N. M. Ribe, and J. T. Browaeys (2004), D-Rex, a program for calculation of seismic anisotropy due to crystal lattice preferred orientation in the convective upper mantle, *Geophys. J. Int.*, *158*(2), 744–752, doi:10.1111/j.1365-246X.2004.02308.x.

Karato, S., M. S. Paterson, and J. D. FitzGerald (1986), Rheology of synthetic olivine aggregates: Influence of grain size and water, *J. Geophys. Res.*, *91*, 8151–8176.

Karato, S.-i., H. Jung, I. Katayama, and P. Skemer (2008), Geodynamic significance of seismic anisotropy of the upper mantle: New insights from laboratory studies, *Annu. Rev. Earth Planet. Sci.*, *36*, 59–95, doi:10.1146/annurev.earth.36.031207.124120.

Keefner, J. W., S. J. Mackwell, D. L. Kohlstedt, and F. Heidelbach (2011), Dependence of dislocation creep of dunite on oxygen fugacity: Implications for viscosity variations in Earth's mantle, *J. Geophys. Res.*, *116*, B05201, doi:10.1029/2010JB007748.

Kneller, E. A., and P. E. van Keken (2007), Trench-parallel flow and seismic anisotropy in the Mariana and Andean subduction systems, *Nature*, *450*(7173), 1222–1225, doi:10.1038/nature06429.

Knoll, M., A. Tommasi, R. E. Logé, and J. W. Signorelli (2009), A multiscale approach to model the anisotropic deformation of lithospheric plates, *Geochem. Geophys. Geosyst.*, *10*, Q08009, doi:10.1029/2009GC002423.

Lassak, T. M., M. J. Fouch, C. E. Hall, and É. Kaminski (2006), Seismic characterization of mantle flow in subduction systems: Can we resolve a hydrated mantle wedge?, *Earth Planet. Sci. Lett.*, *243*(3), 632–649, doi:10.1016/j.epsl.2006.01.022.

Lebensohn, R., and C. Tomé (1993), A self-consistent anisotropic approach for the simulation of plastic deformation and texture development of polycrystals: Application to zirconium alloys, *Acta Metall. Mater.*, *41*(9), 2611–2624, doi:10.1016/0956-7151(93)90130-K.

Li, Z. H., J. F. Di Leo, and N. M. Ribe (2014), Subduction-induced mantle flow, finite strain and seismic anisotropy: Numerical modeling, *J. Geophys. Res. Solid Earth*, *119*, 5052–5076, doi:10.1002/2014JB010996.

Long, M. D., and P. G. Silver (2009), Mantle flow in subduction systems: The subslab flow field and implications for mantle dynamics, *J. Geophys. Res.*, *114*, B10312, doi:10.1029/2008JB006200.

Mainprice, D. (1990), A fortran program to calculate seismic anisotropy from the lattice preferred orientation of minerals, *Comput. Geosci.*, *16*(3), 385–393, doi:10.1016/0098-3004(90)90072-2.

Mainprice, D. (2015), 2.20—Seismic anisotropy of the deep earth from a mineral and rock physics perspective, in *Treatise on Geophysics*, 2nd ed., edited by G. Schubert, pp. 487–538, Elsevier, Oxford, U. K.

Mainprice, D., R. Hielscher, and H. Schaeben (2011), Calculating anisotropic physical properties from texture data using the MTEX open-source package, *Geol. Soc. Spec. Publ.*, *360*(1), 175–192, doi:10.1144/SP360.10.

Mainprice, D., F. Bachmann, R. Hielscher, and H. Schaeben (2014), Descriptive tools for the analysis of texture projects with large datasets using MTEX: Strength, symmetry and components, *Geol. Soc. Spec. Publ.*, *409*, doi:10.1144/SP409.8.

McKenzie, D. (1979), Finite deformation during fluid flow, *Geophys. J. R. Astron. Soc.*, *58*(3), 689–715, doi:10.1111/j.1365-246X.1979.tb04803.x.

Molinari, A., G. R. Canova, and S. Azhy (1987), A self-consistent approach of the large deformation crystal polycrystal viscoplasticity, *Acta Metall.*, *35*, 2983–2994, doi:10.1016/0001-6160(87)90297-5.

Morales, L. F. G., and A. Tommasi (2011), Composition, textures, seismic and thermal anisotropies of xenoliths from a thin and hot lithospheric mantle (Summit Lake, southern Canadian Cordillera), *Tectonophysics*, *507*(1), 1–15, doi:10.1016/j.tecto.2011.04.014.

Nicolas, A., and N. I. Christensen (1987), Formation of anisotropy in upper mantle peridotites—A review, in *Composition, Structure and Dynamics of the Lithosphere-Astenosphere System*, edited by K. Fuchs and C. Froidevaux, AGU, Washington, D. C.

Nicolas, A., F. Boudier, and A. M. Boullier (1973), Mechanism of flow in naturally and experimentally deformed peridotites, *Am. J. Sci.*, *273*, 853–876.

Paczkowski, K., L. G. Montési, M. D. Long, and C. J. Thissen (2014), Three-dimensional flow in the subslab mantle, *Geochem. Geophys. Geosyst.*, *15*, 3989–4008, doi:10.1002/2014GC005441.

Raterron, P., F. Detrez, O. Castelnau, C. Bollinger, P. Cordier, and S. Merkel (2014), Multiscale modeling of upper mantle plasticity: From single-crystal rheology to multiphase aggregate deformation, *Phys. Earth Planet. Inter.*, *228*, 232–243, doi:10.1016/j.pepi.2013.11.012.

Ribe, N. M., and Y. Yu (1991), A theory for plastic deformation and textural evolution of olivine polycrystals, *J. Geophys. Res.*, *96*, 8325–8335.

Sachs, G. (1928), Plasticity problems in metals, *Trans. Faraday Soc.*, *24*, 84–92, doi:10.1039/TF9282400084.

Savransky, D., and N. J. Kasdin (2012), An efficient method for extracting Euler angles from direction cosine matrices, Unpublished manuscript. [Available at (http://spaceisbig.net/docs/findEulerAngs.pdf).]

Skemer, P., and S.-i. Karato (2008), Sheared lherzolite xenoliths revisited, *J. Geophys. Res.*, *113*, B07205, doi:10.1029/2007JB005286.

Skemer, P., I. Katayama, Z. Jiang, and S.-i. Karato (2005), The misorientation index: Development of a new method for calculating the strength of lattice-preferred orientation, *Tectonophysics*, *411*(1), 157–167, doi:10.1016/j.tecto.2005.08.023.

Skemer, P., J. M. Warren, P. B. Kelemen, and G. hirth (2010), Microstructural and Rheological Evolution of a Mantle Shear Zone, *J. Petrol.*, *51*(1-2), 43–53, doi:10.1093/petrology/egp057.

Skemer, P., M. Sundberg, G. Hirth, and R. Cooper (2011), Torsion experiments on coarse-grained dunite: Implications for microstructural evolution when diffusion creep is suppressed, *Geol. Soc. Spec. Publ.*, *360*(1), 211–223, doi:10.1144/SP360.12.

Skemer, P., J. M. Warren, and G. Hirth (2012), The influence of deformation history on the interpretation of seismic anisotropy, *Geochem. Geophys. Geosyst.*, *13*, Q03006, doi:10.1029/2011GC003988.

Signorelli, J., and A. Tommasi (2015), Modeling the effect of subgrain rotation recrystallization on the evolution of olivine crystal preferred orientations in simple shear, *Earth Planet. Sci. Lett.*, *430*, 356–366.

Taylor, G. I. (1938), Plastic strain in metals, *J. Inst. Met.*, *62*, 307–324.

Tommasi, A. (1998), Forward modeling of the development of seismic anisotropy in the upper mantle, *Earth Planet. Sci. Lett.*, *160*, 1–13, doi:10.1016/S0012-821X(98)00081-8.

Tommasi, A., B. Tikoff, and A. Vauchez (1999), Upper mantle tectonics: Three-dimensional deformation, olivine crystallographic fabric and seismic properties, *Earth Planet. Sci. Lett.*, *168*, 173–186, doi:10.1016/S0012-821X(99)00046-1.

Tommasi, A., D. Mainprice, G. Canova, and Y. Chastel (2000), Viscoplastic self-consistent and equilibrium-based modeling of olivine lattice preferred orientations: Implications for upper mantle seismic anisotropy, *J. Geophys. Res.*, *105*, 7893–7908, doi:10.1029/1999JB900411.

Tommasi, A., A. Vauchez, and D. A. Ionov (2008), Deformation, static recrystallization, and reactive melt transport in shallow subcontinental mantle xenoliths (Tok Cenozoic volcanic field, SE Siberia), *Earth Planet. Sci. Lett.*, *272*(1–2), 65–77, doi:10.1016/j.epsl.2008.04.020.

Tommasi, A., M. Knoll, A. Vauchez, J. W. Signorelli, C. Thoraval, and R. Loge (2009), Structural reactivation in plate tectonics controlled by olivine crystal anisotropy, *Nat. Geosci.*, *2*(6), 423–427, doi:10.1038/ngeo528.

Van der Wal, D., P. Chopra, M. Drury, and J. F. Gerald (1993), Relationships between dynamically recrystallized grain size and deformation conditions in experimentally deformed olivine rocks, *Geophys. Res. Lett.*, *20*, 1479–1482.

Vauchez, A., F. Dineur, and R. Rudnick (2005), Microstructure, texture and seismic anisotropy of the lithospheric mantle above a mantle plume: Insights from the Labait volcano xenoliths (Tanzania), *Earth Planet. Sci. Lett.*, *232*(3), 295–314, doi:10.1016/j.epsl.2005.01.024.

Vollmer, F. W. (1990), An application of eigenvalue methods to structural domain analysis, *Geol. Soc. Am. Bull.*, *102*(6), 786–791, doi: 10.1130/0016-7606(1990)102 < 0786:AAOEMT>2.3.CO;2.

Warren, J. M., and G. Hirth (2006), Grain size sensitive deformation mechanisms in naturally deformed peridotites, *Earth Planet. Sci. Lett.*, *248*(1–2), 438–450, doi:10.1016/j.epsl.2006.06.006.

Warren, J. M., G. Hirth, and P. B. Kelemen (2008), Evolution of olivine lattice preferred orientation during simple shear in the mantle, *Earth Planet. Sci. Lett.*, *272*(3–4), 501–512, doi:10.1016/j.epsl.2008.03.063.

Webber, C., J. Newman, C. W. Holyoke III, T. Little, and B. Tikoff (2010), Fabric development in cm-scale shear zones in ultramafic rocks, Red Hills, New Zealand, *Tectonophysics*, *489*(1), 55–75, doi:10.1016/j.tecto.2010.04.001.

Wendt, A. S., D. Mainprice, E. Rutter, and R. Wirth (1998), A joint study of experimental deformation and experimentally induced microstructures of pretextured peridotites, *J. Geophys. Res.*, *103*, 18,205-18,221.

Wenk, H. R., K. Bennett, G. R. Canova, and A. Molinari (1991), Modelling plastic deformation of peridotite with the self-consistent theory, *J. Geophys. Res.*, *96*, 8337–8349.

Wheeler, J. (2009), The preservation of seismic anisotropy in the Earth's mantle during diffusion creep, *Geophys. J. Int.*, *178*(3), 1723–1732, doi:10.1111/j.1365-246X.2009.04241.x.

Zhang, S., and S.-i. Karato (1995), Lattice preferred orientation of olivine aggregates deformed in simple shear, *Nature*, *375*(6534), 774–777, doi:10.1038/375774a0.

Zhang, S., S.-i. Karato, J. Fitzgerald, U. H. Faul, and Y. Zhou (2000), Simple shear deformation of olivine aggregates, *Tectonophysics*, *316*, 133–152, doi:10.1016/S0040-1951(99)00229-2.